nature structural & molecular biology

Article

https://doi.org/10.1038/s41594-025-01593-7

P-type ATPase magnesium transporter MgtA acts as a dimer

Received: 21 December 2023

Accepted: 8 May 2025

Rilee Zeinert[1], Fei Zhou[2], Pedro Franco[3], Jonathan Zöller[3], Zaid K. Madni[2], Henry Lessen[4], L. Aravind[5], Julian D. Langer[3], Alexander J. Sodt[4] ✉, Gisela Storz[1] ✉ & Doreen Matthies[2] ✉

Magnesium (Mg^{2+}) uptake systems are present in all domains of life, consistent with the vital role of this ion. P-type ATPase Mg^{2+} importers are required for bacterial growth when Mg^{2+} is limiting or during pathogenesis. However, insights into their mechanisms of action are missing. Here we solved the cryo-EM structure of the Mg^{2+} transporter MgtA from *Escherichia coli*. We obtained high-resolution structures of both homodimeric (2.9 Å) and monomeric (3.6 Å) forms. The dimer structure is formed by multiple contacts between residues in adjacent soluble N and P subdomains. Our structures revealed an ion, assigned as Mg^{2+}, in the transmembrane segment. Moreover, we detected two cytoplasmic ion-binding sites and determined the structure of the N-terminal tail. Sequence conservation, mutagenesis and ATPase assays indicate dimerization, the ion-binding sites and the N-terminal tail facilitate cation transport or serve regulatory roles.

Magnesium (Mg^{2+}) is an essential divalent cation supporting core biological processes through its interactions with polyphosphate compounds such as ATP and its roles in enzyme catalysis. In bacteria, Mg^{2+} translocation across the plasma membrane is carried out by the CorA and MgtE families of channel proteins and the CorB/C and MgtA/B families of transporters[1–3]. Bacterial CorA and MgtE are constitutively expressed and are required for maintenance of intracellular levels of Mg^{2+} (ref. 1). When Mg^{2+} becomes less abundant, as during an infection, the homologous MgtA and MgtB transporters (Fig. 1a and Extended Data Fig. 1) are induced to ensure maintenance of adequate intracellular Mg^{2+} concentrations[4]. Consistent with this induction, MgtA is required for growth under low Mg^{2+} conditions in *Escherichia coli*, and deletion of *Salmonella enterica mgtB* results in decreased bacterial survival in macrophages and in reduced pathogenicity[5–9].

MgtA and MgtB are members of the broader family of P-type ATPases that use ATP hydrolysis to fuel the transport of numerous biologically important transition metals, as well as heavy metals and lipids[10]. They share a high degree of sequence similarity (Extended Data Fig. 2a), particularly of functionally significant residues (Extended Data Fig. 2b) and, based on AlphaFold[11,12], are predicted to be structurally similar. MgtA belongs to the P-type ATPase subfamily 3B and is a sister clade of the 3A subfamily of proton pumps found in fungi, plants and some archaea (Extended Data Fig. 2a). Of the vertebrate P-type ATPases, those from the Ca^{2+} transporting clade, including the Ca^{2+}/Mn^{2+}-transporter SPCA1 (encoded by *ATP2C1A*) implicated in the skin disease Hailey–Hailey and the extensively-studied Ca^{2+}-pump SERCA (encoded by *ATP2A1*) mutated in Brody's myopathy, are the closest to MgtA in sequence.

P-type ATPases use a highly conserved post-Albers cycle mechanism involving E1 and E2 states to coordinate transport of their respective ions across the membrane (Fig. 1b)[10,13,14]. The transition between E1 and E2 states is induced by ligand binding and ATP cleavage with transfer of the γ-phosphate to an aspartate within the conserved DKTGT consensus motif (D373 in *E. coli* MgtA)[15]. For MgtA, a D373N substitution abolished ATP hydrolysis in vitro, emphasizing its importance in the catalytic cycle[16]. Upon ion translocation, the aspartate is dephosphorylated by a glutamic acid (E215 in *E. coli* MgtA) from the TGES loop in the soluble A domain, and the protein returns to the E1 state[17].

---

[1]Division of Molecular and Cellular Biology, Eunice Kennedy Shriver National Institute of Child Health and Human Development, National Institutes of Health, Bethesda, MD, USA. [2]Unit on Structural Biology, Eunice Kennedy Shriver National Institute of Child Health and Human Development, National Institutes of Health, Bethesda, MD, USA. [3]Max Planck Institute of Biophysics, Frankfurt, Germany. [4]Section on Membrane Chemical Physics, Eunice Kennedy Shriver National Institute of Child Health and Human Development, National Institutes of Health, Bethesda, MD, USA. [5]National Center for Biotechnology Information, National Institutes of Health, Bethesda, MD, USA. ✉e-mail: alexander.sodt@nih.gov; storzg@mail.nih.gov; doreen.matthies@nih.gov

https://doi.org/10.1038/s41594-025-01593-7

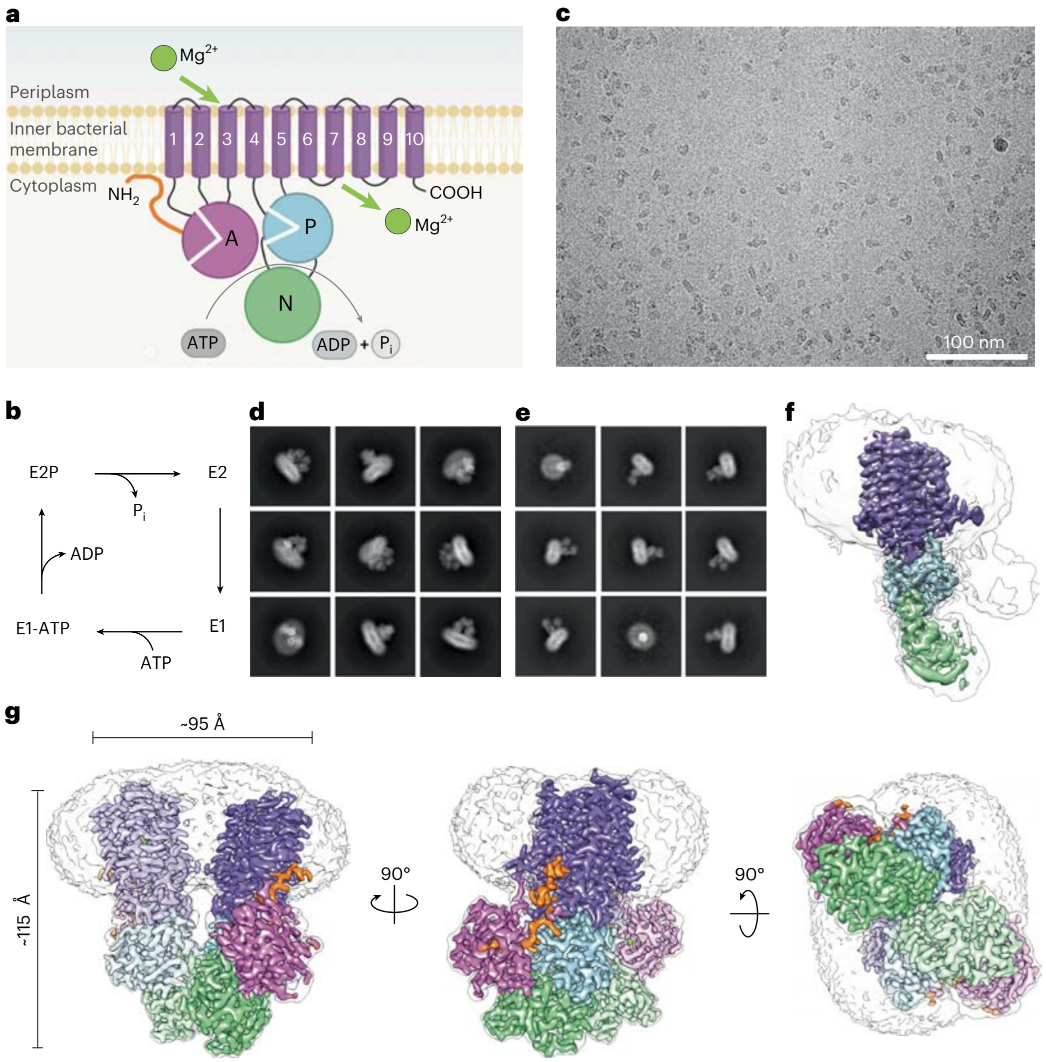

Fig. 1 | Cryo-EM of Mg^{2+} transporter MgtA reveals a high-resolution dimer and a monomeric structure. a, A schematic representation of MgtA/B based on P-type ATPase structural homology predicting ten conserved TM helices colored in purple (1–10), the actuator (A) domain in orchid, the phosphorylation (P) subdomain in light blue, the nucleotide (N) binding or CAP subdomain in light green and the predicted unstructured N-terminal tail in orange. The A domain is split into two regions a/b. The b segment of the A domain comprises a double-stranded β-helix fold. The soluble P subdomain is a noncontiguous segment comprised of two regions a/b that house the key catalytic residues required for phosphorylation. The N subdomain binds the nucleotide and aids in catalysis. The P and N subdomains together comprise the HAD domain[20]. **b**, Post-Albers reaction scheme indicating the typical cytoplasmic side-open (E1), ATP-bound cytoplasmic side-open (E1-ATP), periplasmic side-open (E2P) and ion-occluded (E2) states. **c**, Representative micrograph of purified *E. coli* MgtA. Representative image of the $n > 17{,}000$ total micrographs. **d**,**e**, Representative final 2D class averages for the ~200 kDa dimer (**d**) and the ~100 kDa monomer (**e**), with a box size of 384 pixels (approximately 319 Å). **f**,**g**, Cryo-EM reconstruction of the MgtA monomer (**f**; also see Supplementary Figs. 2 and 3c,d and Supplementary Video 2) and of the dimer (**g**; also see Supplementary Figs. 2 and 3a,b and Supplementary Video 1). Cryo-EM maps in **f** and **g** are colored as in **a**. A transparent gray map at a much lower threshold indicates the detergent micelle and the map features for the more flexible loops and the A domain in the monomer map. Panel **a** created with BioRender.com.

Many insights into P-type ATPase function have been gained through work on SERCA, including 70 monomeric structures capturing various states of its transport cycle[18]. However, despite the wealth of data about P-type ATPases and the potential clinical relevance of interfering with Mg^{2+} transporters to block infection, there is limited information about the MgtA structure and mechanism of action, with only a single structure of the soluble nucleotide-binding domain[19].

The 100 kDa *E. coli* MgtA protein is predicted to consist of ten transmembrane (TM) α-helices interwoven with cytosolic regions (Fig. 1a and Extended Data Fig. 1). The cytosolic regions include an N-terminal tail, an A (actuator) domain and a double-stranded β-helix fold domain, as well as a catalytic haloacid dehalogenase domain (HAD). The HAD comprises the P (phosphorylation) subdomain, as it bears the reversibly phosphorylatable aspartate, and the CAP subdomain, termed N (nucleotide) as it binds the sugar and base moieties of the nucleotide and excludes water during phosphotransfer[20]. ATP hydrolysis by *E. coli* MgtA is regulated by both Mg^{2+} levels and the presence of the anionic lipid cardiolipin in vitro, and MgtA colocalizes with cardiolipin in vivo[16]. In both *E. coli* and *S. enterica*, the stability of the transporter also is regulated by small proteins of less than 50 amino acids[8,21]. The structural basis for how Mg^{2+} concentration, lipid composition and small proteins modulate MgtA activity and stability is unclear.

Here, we used single-particle cryo-electron microscopy (cryo-EM) to determine the full-length structure of *E. coli* MgtA at an overall resolution of 2.9 Å, illuminating several features of the transporter. We found that MgtA exists as both a dimer and a monomer. Molecular dynamics (MD) simulations in a lipid environment together with sequence conservation and biochemical assays showed the dimer is a stable structure and capable of hydrolyzing ATP. The cryo-EM maps revealed features for three ions we have assigned as Mg^{2+}: one in the TM domain and two between the cytosolic domains. The N-terminus, previously predicted to be disordered, also was resolved in our dimeric structure. Conservation analysis combined with mutagenesis studies revealed residues required for ion transport and possibly regulation, adding insights to the diverse mechanisms by which P-type ATPases are regulated.

Results

MgtA is detected as dimeric and monomeric forms

E. coli MgtA was previously found to bind and be stabilized by the 31 amino acid MgtS protein[21]. We set out to purify this MgtA–MgtS complex. Detergent solubilization of *E. coli* membranes containing both overexpressed proteins revealed that weaker detergents such as glyco-diosgenin (GDN) maintained MgtA–MgtS interactions, while stronger detergents such as *n*-dodecyl-β-ᴅ-maltoside (DDM) and lauryl maltose neopentyl glycol (LMNG) disrupted the hetero-complex (Extended Data Fig. 3a). Intriguingly, LMNG and DDM-solubilized MgtA migrated at ~200 kDa by native PAGE, while GDN-solubilized MgtA migrated at ~400 kDa (Extended Data Fig. 3a–c).

We assessed ATPase rates of our purified MgtA protein and the catalytically inactive D373N mutant solubilized with GDN. Previously, ATPase activity for DDM-extracted MgtA was shown to require exogenous lipids and was strongly inhibited by 1 mM $MgCl_2$ (ref. 16). We found MgtA purified in GDN possessed substantial ATPase activity (~1,500 nmol ATP min^{-1} mg^{-1}) with 0.5 and 10 mM $MgCl_2$, which somewhat increased with 2 and 5 mM $MgCl_2$, but was inhibited at 20 mM $MgCl_2$ even without exogenous lipid addition, though we observed some increase with cardiolipin (Extended Data Fig. 3d–f). No contaminating ATP-hydrolyzing enzymes were present in our sample since no activity was detected for the GDN-solubilized D373N mutant. For our structural studies, we proceeded with protein purified with GDN in the presence of 5 mM $MgCl_2$ given that these conditions preserved native protein–protein interactions and were associated with high ATPase activity.

Negative-staining electron microscopy (EM) showed that the purified sample was homogeneous, containing individual particles of the expected size of ~8–11 nm (Supplementary Fig. 1). Cryo-EM images of purified MgtA (Fig. 1c) revealed particles of sizes between ~7 and 11 nm. Two-dimensional (2D) class averages showed particles with larger (Fig. 1d) and smaller (Fig. 1e) detergent micelles consistent with the two forms of the transporter detected by native PAGE (Extended Data Fig. 3) and negative-staining EM (Supplementary Fig. 1). The characteristic soluble A and HAD (containing N and P subdomains) domains were visible for some side view 2D class averages (Fig. 1e and Supplementary Fig. 1d). The final dimer maps obtained here had an overall resolution of 2.9 Å (C2) and 3.0 Å (C1) with local resolutions ranging from ~2.2 to ~3.5 Å (Fig. 1g, Extended Data Fig. 4, Supplementary Figs. 2 and 3 and Supplementary Video 1). The final monomer map had an overall resolution of 3.65 Å, with local resolutions ranging from ~2.8 to ~7 Å (Fig. 1f, Supplementary Figs. 2 and 3 and Supplementary Video 2). The lowest resolution corresponded to the A domain, indicating a high degree of flexibility of that region. None of the maps revealed densities for the small protein MgtS, possibly due to dissociation during sample preparation or few homogeneous MgtA–MgtS particles. We thus focused on features of MgtA.

We observed extra densities corresponding to detergent micelles in the raw EM images and 2D class averages (Fig. 1c–e) as well as the cryo-EM maps (Fig. 1f,g and Extended Data Fig. 5a). The locations of the inner and outer lipid membrane leaflet could be inferred from the elongated densities corresponding to detergents or copurified lipids detected directly adjacent to the TM α-helices. However, the local resolution was insufficient to assign a molecular identity. The hydrophobic regions of the TM segments and the border of the inner lipid membrane leaflet could be discerned from the electrostatic potential surface representation of the final structural model as well as by the hydrophobic region of the bilayer in the MD simulation (Extended Data Fig. 5b). MD simulations in conditions that mimic the native lipid environment revealed several arginine and lysine residues that were in contact with the headgroups of anionic lipids for more than 20% of the simulation (Extended Data Fig. 5b–d), with R893/R894 making multiple contacts for the duration of the simulation. Interestingly, cardiolipin was found to migrate toward the transporter during the simulation (Extended Data Fig. 5e).

To complement our structural analysis, we treated GDN-solubilized MgtA with a zero-length crosslinker and identified crosslinked residues by mass spectrometry (MS) (Supplementary Fig. 4). Based on the dimeric structure, the distances between the crosslinked residues ranged from 3.5 to 45.5 Å. The crosslinks of <10 Å were consistent with nearby residues in our final dimeric reconstruction. Most long-range crosslinks (>20 Å) were between the end of the TM α-helix 2 (K144) and the A domain or P subdomains and could indicate multiple conformational states especially since the A domains of P-type ATPases undergo large structural rearrangements during the transport cycle. However, it is possible that some of the crosslinks occurred between neighboring molecules.

MgtA monomer is more splayed than the dimer

The root mean squared deviation (RMSD) comparison and morphing between monomer and dimer (Extended Data Fig. 6 and Supplementary Video 3) showed the greatest differences in the A domain, but several other notable differences were also observed. The TM1 and TM2 α-helices in the monomer structure moved by ~1.5 helix turns toward the cytoplasm (Extended Data Fig. 6d,e), possibly due to the A domain rotation. TM4, which harbors E331, comprising a well-conserved canonical binding site (CBS) found to coordinate ions in other P-type ATPases, appears to unwind in the monomeric structure allowing E331 to rotate (Extended Data Fig. 6f). The A domain and P and N subdomains also all move farther away from each other in the monomer structure, adopting a more splayed structure (Extended Data Fig. 6c,h–j).

Superposition of the monomer and dimer structures on other P-type ATPases revealed that the extended configuration of the cytosolic domains as well as the position of TM1–4 in the monomer are structurally similar to assigned E2P and E2 states of the Ca^{2+}-pump SERCA (Protein Data Bank (PDB) 3N5K (ref. 22), PDB 2EAR (ref. 23) and PDB 3NAL (ref. 24)). In contrast, the closest structural similarity of each monomer subunit in the dimer was with assigned E1 states of H^+ pump PmaI (PDB 7NXF (ref. 25)), H^+ pump (encoded by *AHA2*) (PDB 5KSD (ref. 26)) and Ca^{2+}/Mn^{2+}-ATPase SPCA1a (PDB 7YAH (ref. 27)).

MgtA dimer structure is stable

The dimer interface of MgtA is composed of salt bridges, hydrogen bonding between polar residues and hydrophobic contacts between the N and P subdomains of neighboring MgtA subunits (Fig. 2a and Supplementary Table 1). The TM domains do not appear to be involved in dimerization since the closest distance between the two subunits in the TM region is ~8 Å (between I839 in TM9 of each monomer). While MD simulations cannot easily assess the absolute stability of an interface, they can indicate the dynamic nature of interactions, probably correlating with stability. Electrostatic and polar interaction partners were all closely positioned and persistent throughout the simulation of 2 µs (Q380–Q380 87%, N387–Q508 63%, K548–E549 88% and K382–E582 64%; Supplementary Table 1). Our simulations also revealed an additional transiently (17%) populated salt bridge (E386–K578) that was not present in our structure. The hydrophobic interface was intact throughout the entire simulation (Supplementary Videos 4 and 5). The dimer interface residues are well conserved among MgtA and MgtB family members but less so in the mammalian homolog SERCA and not at all in distantly related P-type ATPase proteins (Extended Data Fig. 2).

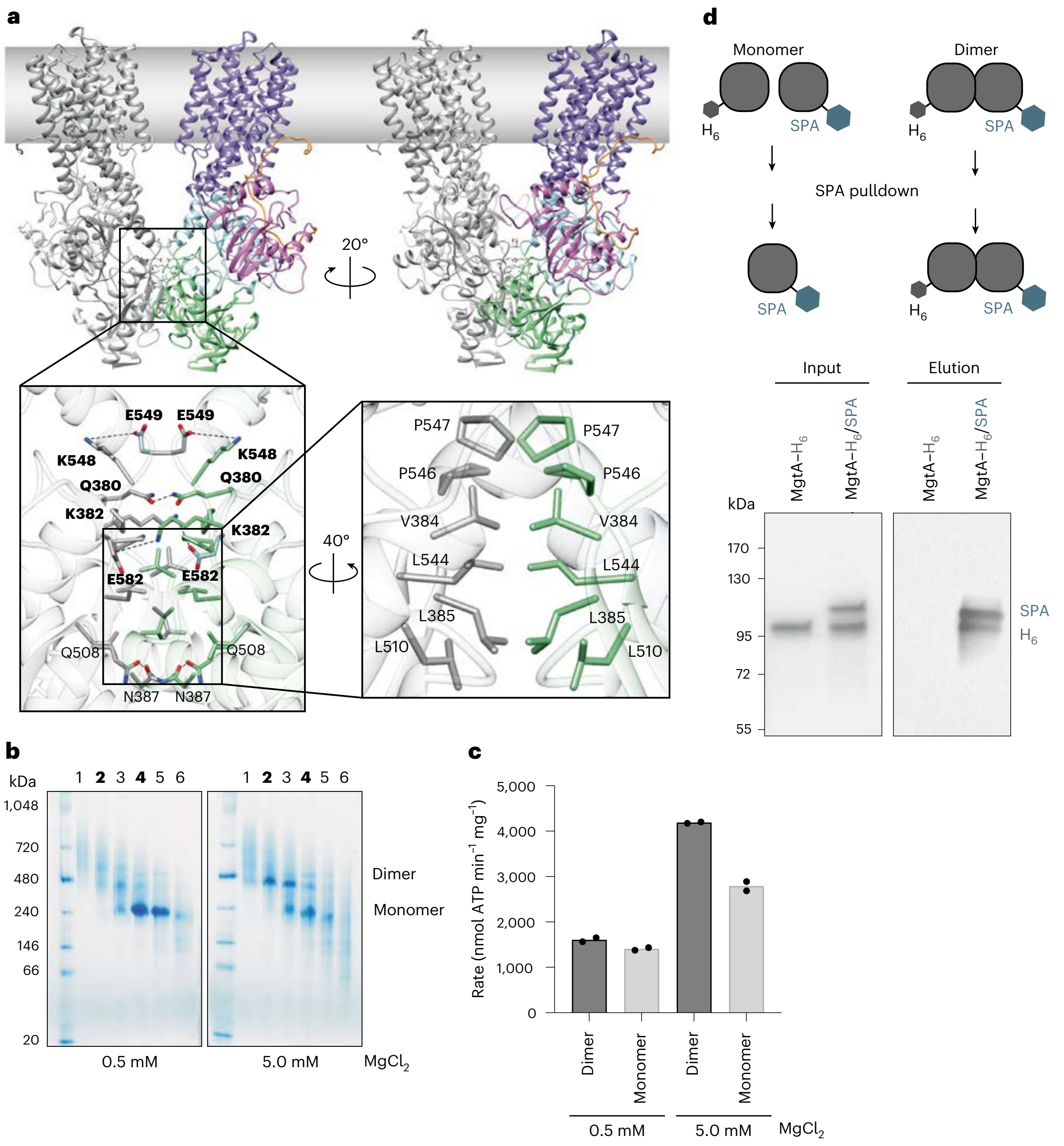

Fig. 2 | The dimer interface is formed by both hydrophobic and polar interactions. a, Side view of the overall dimer structure with the left monomer in gray and the right monomer colored as in Fig. 1. A close-up view of the extensive dimer interface between the two N and P subdomains with sidechain residues displaying charged interactions across the dimer interface is shown below. Rotation of the structure highlights hydrophobic interactions at the dimer interface. MD simulations (Supplementary Videos 4 and 5) show consistent interactions across the dimer interface between K382–E582 (64%), Q380–Q380 (87%) and K548–E549 (88%) shown in bold. **b**, Native PAGE gel of SEC fractions 1–6 following Superose 6 Increase 10/300 GL. Bolded fractions 2 and 4 for 0.5 and 5 mM $MgCl_2$ were used in ATPase assays. **c**, ATPase activity of dimer and monomer fractions purified in low and high Mg^{2+} conditions. The assays were performed with 6.25 µg of MgtA and 2 mM ATP at 37 °C and the phosphate released was quantified using molybdate/malachite green-based assays. Data are shown for duplicate experiments with mean. **d**, Copurification of two differentially tagged MgtA derivatives, one tagged with H_6 and the other tagged with the larger SPA tag as shown in the top schematic reveals copurification of the two proteins (right elution image). The experiment was performed twice with consistent results. Proteins were visualized by western blot analysis using MgtA antibodies.

To test whether dimerization was influenced by the Mg^{2+} present during the purification, MgtA was solubilized and purified in the presence of 0.5 or 5 mM $MgCl_2$. Native PAGE analysis of normalized protein samples revealed that more dimer was present for MgtA purified with higher $MgCl_2$ (Fig. 2b). In ATPase activity assays of predominantly dimer or monomer fractions for both $MgCl_2$ concentrations, we observed that dimer fractions possessed slightly higher ATPase rates than monomer fractions in 5 mM $MgCl_2$, while the hydrolysis rates for the protein purified in 0.5 mM $MgCl_2$ were similarly low (Fig. 2c). Attempts to disrupt the dimer interface by mutagenesis failed despite introducing many mutations along the interface (Supplementary Table 2). We also grew cells expressing low levels of both MgtA with a small H_6 tag and MgtA with a large SPA tag and found when we purified MgtA–SPA from cells expressing both proteins, the elution fraction contained MgtA–SPA and MgtA–H_6 at a nearly equal ratio (Fig. 2d). Together these data suggest that the purified dimer is stable in vivo and in vitro, the ratio of purified MgtA monomer to dimer is influenced by the concentration of Mg^{2+}, and dimerization does not inhibit ATPase activity.

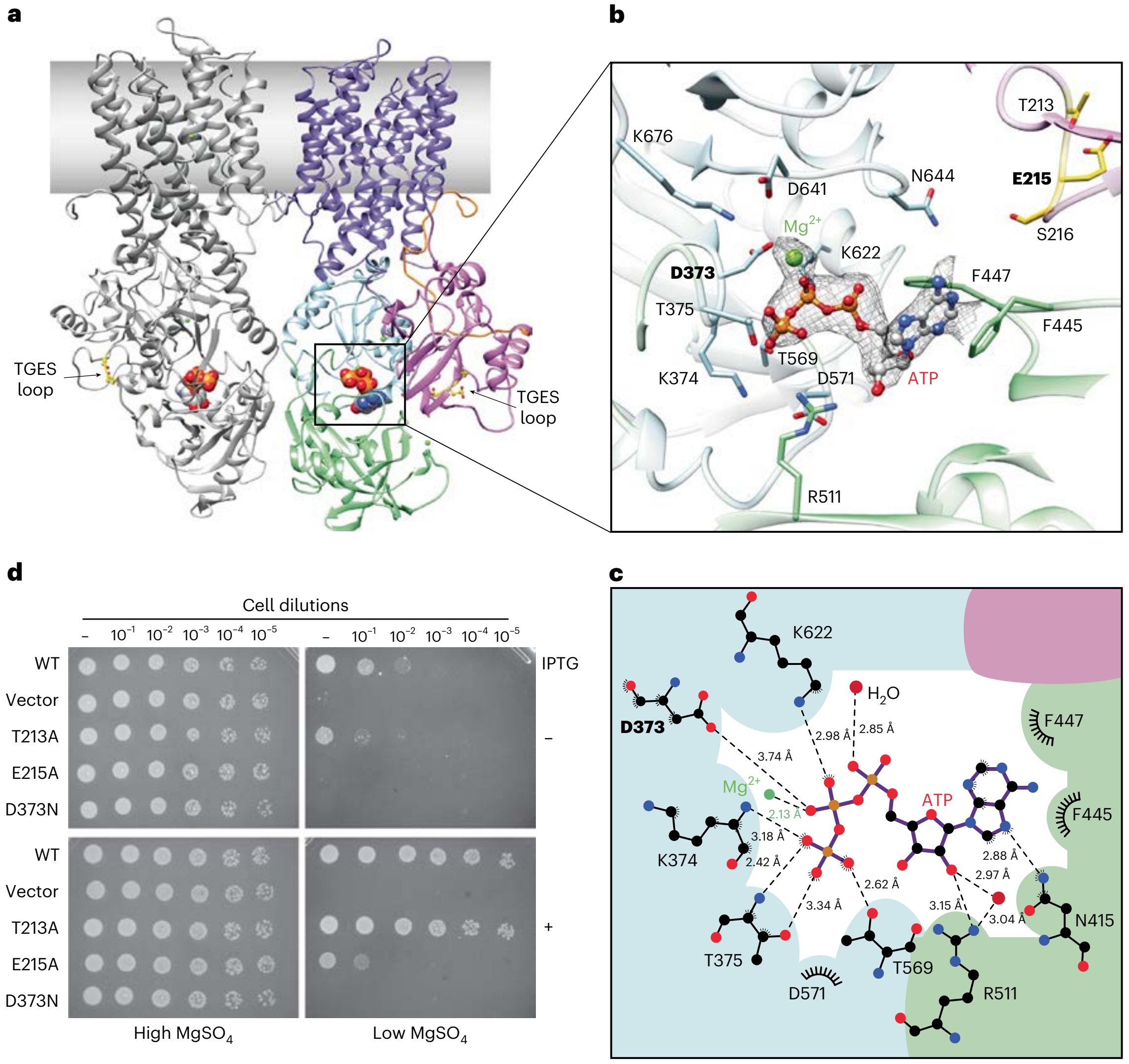

Fig. 3 | The nucleotide binding pocket of MgtA is accessible in the dimeric state. **a**, A side view of the MgtA dimer with the left monomer in gray and the right monomer colored as in Fig. 1, highlighting the ATP molecule represented in spheres located in between the soluble A domain and P and N subdomains and the dephosphorylation TGES loop in yellow. **b**, A close-up view of the ATP-binding site highlighting residues in close proximity to the Mg-ATP molecule, which is shown in a ball and stick representation and the cryo-EM map in gray mesh. Residues from the TGES loop involved in dephosphorylation and located in the A domain are colored yellow. N415 is omitted for a better view of the site. **c**, Distances from ATP to amino acids, water molecules and Mg^{2+} ion in the nucleotide binding pocket of MgtA from *E. coli*, determined using LIGPLOT+[57]. **d**, The D373N mutant is unable to complement a Mg^{2+}-auxotrophic *E. coli* strain, indicating this mutant transporter does not import Mg^{2+} ions. The D373 residue becomes phosphorylated upon ATP hydrolysis. The E215A mutant is only partially able to complement upon overexpression. The E215 residue is part of the TGES loop involved in dephosphorylation. Overnight cultures were serial diluted and spotted onto LB agar plates supplemented with high (100 mM) or low (1 mM) $MgSO_4$ with (+) and without (−) 0.1 mM IPTG for induction and grown at 37 °C (see replicate and protein levels at ref. 58).

MgtA dimer can bind ATP

We also solved structures of dimeric MgtA (Extended Data Fig. 3c) with Mg^{2+} and either ATP, nonhydrolyzable ATPγS or ADP. Despite the presence of extra map features at the conserved nucleotide-binding sites in our maps, no large structural rearrangements occurred upon nucleotide binding (Supplementary Fig. 5). The ATP-binding site, resolved locally at 2.9–3.2 Å, is highly similar to other P-type ATPases (Fig. 3a–c, Supplementary Figs. 5 and 6 and Supplementary Video 6). Unique to the MgtA–MgtB clade is F447, which contacts the adenine ring of the ATP on the opposite side of the conserved F445 residue (Fig. 3b,c). MD simulations of ATP binding sampled a range of conformations in our MgtA–ATP structure (Supplementary Fig. 6) with fluctuating interactions of the ATP phosphates with other residues (Supplementary Table 3). Hydrogen deuterium exchange MS (HDX–MS) showed the biggest differences in deuterium uptake with ATP and ATPγS are in the N and P subdomains, with a decrease in uptake observed in several peptide stretches containing residues required for ATP binding (Supplementary Fig. 7) consistent with our cryo-EM and MD simulation data. Collectively, these data show that the dimer can bind the nucleotides similar to other P-type ATPases.

To assess the in vivo function of the DKTGT motif and the TGES dephosphorylation loop, we introduced a D373N mutation in the DKTGT motif, previously shown to abolish ATP hydrolysis in vitro[16] (Extended Data Fig. 3f), and T213A and E215A substitutions in the TGES loop. We assayed the ability of the mutants to complement an *E. coli* strain deficient in all endogenous Mg^{2+} uptake systems, which requires Mg^{2+} supplementation or a functional Mg^{2+} uptake system for growth[9]. Under low Mg^{2+} conditions, wild-type (WT) MgtA and the T213A mutant were capable of supporting growth upon induction with isopropyl-β-D-1-thiogalactopyranoside (IPTG) (Fig. 3d). In contrast, the D373N mutant did not grow and the E215A mutant had notably less growth without $MgSO_4$ supplementation (Fig. 3d), despite being stably expressed. Thus, D373 and E215 have important roles in the MgtA transport mechanism.

Multiple ion-binding sites are detected in MgtA

Our cryo-EM maps for dimeric MgtA show extra densities that we assigned to three Mg^{2+} ions (denoted sites A, B and C) given our functional characterization of these sites below (Fig. 4). We note that, since our buffers contained high concentrations of potassium (K^+), there is a possibility that one or more of the sites might be occupied by K^+. However, the Mg^{2+} assignments are supported by enhanced MD simulations showing K^+ is bound substantially less strongly in site A (by over 5 kcal mol^{-1}), along with equilibrium simulations showing K^+ spontaneously leaving and returning to sites A, B and C with average occupancy below 70% compared with 100% occupancy for Mg^{2+} (Extended Data Fig. 7a).

Site A comprises neighboring polar residues D780, N709, S776 and S813 residing in the middle of TM helices 5, 7 and 8, along with three nearby molecules likely to be water (Fig. 4a). This Mg^{2+} feature was observed at the same location in the MgtA monomer map (Extended Data Fig. 6g) and all three nucleotide-bound dimer structures (Supplementary Fig. 5d). The presence of Mg^{2+} in the E1-like MgtA dimer appears to be in contradiction to our structural state assignment since other P-type ATPases in the E1 state are ion free or releasing the ion ('Discussion'). It is possible the Mg^{2+} binding at site A is stabilizing or regulatory. Sequence conservation analysis comparing the MgtA clade and the SERCA Ca^{2+} clade revealed that residue D780 is exclusively present in the Mg^{2+}-transporter clade (Extended Data Fig. 7b). While MgtA has the well-conserved CBS comprising residues E331 and D738, no ion could be observed at this site in any of our cryo-EM maps. However, consistent with the importance of both E331 and D780, alanine substitutions at these positions prevented complementation of the transport-deficient strain (Fig. 4c). D738 appears to be less critical given that a D738A mutant could partially complement growth (Fig. 4c). The D780A mutant purified in the presence of 5 mM $MgCl_2$ was still capable of forming dimers (Fig. 4e) and hydrolyzing ATP (Fig. 4f). Thus, this mutant is likely to be properly folded and inserted into the membrane, but unable to import Mg^{2+}. The strong growth phenotype, even with full ATPase activity, is consistent with D780 directly or indirectly being involved in ion transport across the membrane bilayer.

We traced resolved waters in our structure and in our simulations to look for a path that could support the hydration of the TM Mg^{2+} ion during transport (Extended Data Fig. 8). A snapshot of the region after one microsecond of simulation shows that this timeframe is sufficient to hydrate the TM interior. A short water path terminates near TM6 with only transient connections of a single-water channel width to the periplasmic aqueous layer. A notable water chamber terminates near E331 in TM4 without sufficient width to maintain continuous hydration of Mg^{2+} all the way to the cytoplasmic aqueous layer. Transient, narrow connections to the cytoplasmic side were formed more frequently (47% without ATP, 33% with ATP and 8% for the monomer) than to the periplasmic side (7% with ATP and none without); however, overall there is no clear access of the TM Mg^{2+} to the cytoplasm or periplasm.

The soluble ion-binding site B is formed by P subdomain D663, A domain D191, T156, T158 and E173 along with nearby water molecules, while site C is formed by N subdomain D441 and D526, A domain D204 and E220 along with neighboring water molecules (Fig. 4a and Extended Data Fig. 4). Enhanced sampling simulations perturbing each Mg^{2+} from its aspartic acid binding residue indicate similar binding affinities (a 15 kcal mol^{-1} barrier to dissociate) (Extended Data Fig. 7a). We assessed the ability of mutants with substitutions at site B (D191A and D663A) and site C (E220A and D441A) to support growth of the Mg^{2+} uptake deficient strain. The site B mutants D191A and D663A and the site C mutant E220A all allowed growth at low Mg^{2+} concentrations (Fig. 4d). Intriguingly, the site C mutant D441A displayed a notable reduction in growth under low Mg^{2+} (Fig. 4d). Given the residues that comprise site C are located near F445 and F447 that interact with ATP and residues D204 and E220 that lie on either side of the TGES loop, it is possible this site impacts the ATP hydrolysis cycle. Thus, we further examined the D441A protein. Purified D441A was capable of oligomerizing (Fig. 4e); however, ATP hydrolysis was dramatically reduced (Fig. 4f). Thus, mutation of D441 is not sufficient to disrupt oligomerization but dramatically reduces ATP hydrolysis, impacting the transport cycle.

Structure of MgtA N-terminus suggests a regulatory role

Poorly conserved N-terminal tails are unique to MgtA, several members of the closely related fungal and plant H^+-pumps Pma1/Pma2 and more distantly related Na^+/K^+- and H^+/K^+-ATPases (Extended Data Fig. 9a). For the Na^+/K^+- and H^+/K^+-ATPases, the N-termini have been proposed to be regulatory though the details remain obscure[28]. Previous in vitro studies showed that, in isolation, the N-terminus of MgtA is intrinsically disordered and interacts with anionic lipid vesicles, possibly as a membrane tether[29]. The structure of this segment is uncertain in AlphaFold predictions of MgtA and other P-type ATPases (Extended Data Fig. 9b). However, we observed well-resolved features for the N-terminus in our MgtA dimer map (Figs. 1g and 5 and Extended Data Figs. 4 and 9c) resulting in a structural model that is different from the prediction. The N-terminus covers a negatively charged surface spanning parts of TM2 and TM4, which are thought to be involved in the ion pathway and interacts with cytosolic A and P regions (Fig. 5b and Extended Data Fig. 9d). Interestingly, the N-terminus appears to snorkel under the A domain forming a knot-like structure. Simulations show that the N-terminus adopts a stable, short amphipathic α-helix, consistent with the hydrophobicity of I5 and L9 and charge of K3 and R8, that interact with nearby lipid phosphate moieties (Supplementary Video 8).

While the N-terminus is poorly conserved, it is consistently present and tends to be amphipathic across the MgtA-like clade of Mg^{2+} transporters. In previous studies using DDM to extract MgtA, a derivative lacking the N-terminal 31 amino acids (Δ1–31) had ATPase activity similar to WT MgtA[16]. When we purified the Δ1–31 mutant in GDN, we found it still formed dimers (Extended Data Fig. 9e), and both dimer and monomer fractions had ATPase activity like the WT protein. However, in 20 mM $MgCl_2$, the Δ1–31 dimer fraction had slightly higher activity than the WT dimer fraction, while the Δ1–31 monomer fraction had lower activity (Extended Data Fig. 9f). For MgtA expressed at endogenous levels, truncations and mutations in the N-terminus resulted in decreased stability preventing functional analysis in vivo (Extended Data Fig. 9g). Given the unique configuration, interdomain contacts and interactions with residues comprising the CBS, we hypothesize that the N-terminus may help stabilize a structural state and have a regulatory function.

Discussion

Here, we presented high-resolution structures of the P-type ATPase Mg^{2+} transporter MgtA in dimeric and monomeric states. We also reported structures of dimeric MgtA bound to ATP, ATPγS and ADP revealing MgtA residues involved in nucleotide binding. However, unlike what has been observed for most monomeric P-type ATPase structures, the cytosolic domains did not show large structural changes upon nucleotide addition. We observed an ion assigned as Mg^{2+} surrounded by residues within TM α-helices 5, 7 and 8. Mutational analysis of this site as well as others, chosen on the basis of sequence conservation and ion coordination in other P-type ATPases, resulted in impaired growth under Mg^{2+}-limiting conditions suggesting these residues are involved in ion translocation across the membrane. We also identified two potential cytosolic Mg^{2+}-binding sites, probably of low affinity, which, according to mutational analysis, might function in a regulatory manner. Additionally, this work provides the structure of the

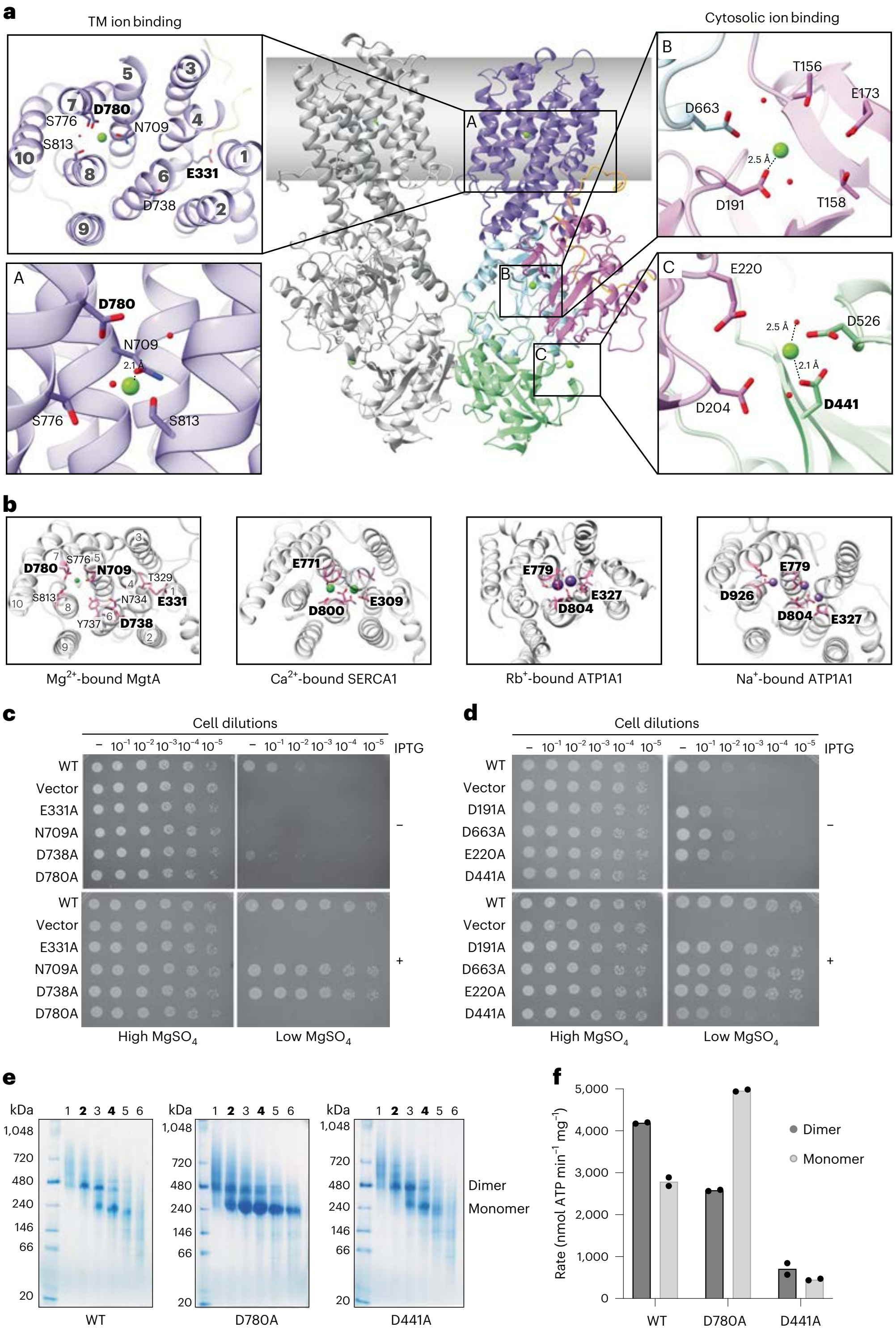

Fig. 4 | Mg^{2+} binds sites in the transmembrane domain and between the cytosolic A domain and N and P subdomains. a, A side view of the dimeric structure with left monomer in gray and right monomer colored as in Fig. 1 and close-up views of the resolved Mg^{2+} ions (green), nearby residues and proximal resolved water molecules (red spheres). The dotted black lines indicate residue distances to Mg^{2+}. **b**, A structural comparison of selected ion-bound P-type ATPases. One subunit of the dimeric EcMgtA transporter is shown with corresponding regions of the SERCA1 Ca^{2+} transporter (PDB 2ZBD)[59] and ATP1A1 Na^+/K^+ transporter with Rb^+ as K^+ congeners (PDB 3B8E)[55] or Na^+ (PDB 4HQJ)[60]. Residues of EcMgtA, SERCA1 and ATP1A1 predicted to be involved in ion binding are colored pink, the Mg^{2+} and Ca^{2+} ions are green and the Rb^+ and Na^+ ions are purple. The residues mutated in MgtA are labeled in bold font. Those residues in SERCA1 and ATP1A1 that are part of the CBS and correspond to the MgtA E331, N709 and D738 are also labeled in bold font. For the ATP1A1 Na^+-bound structure, a Na^+ ion coordinated by D926 is found in a location similar to the Mg^{2+} observed in MgtA. **c**, Mutants with E331A (TM4) or D780A (TM7) are unable to complement a Mg^{2+}-auxotrophic *E. coli* strain. **d**, The D441A (site C) mutant is only partially able to complement the Mg^{2+}-auxotrophic *E. coli* strain upon overexpression. Complementation assays in **c** and **d** were carried out as for Fig. 3d (see replicate and protein levels at ref. 58). **e**, Native PAGE gel of WT and mutants as described in Fig. 2b. Bolded fractions 2 and 4 for WT and D441A and fractions 1 and 5 for D780A were used for ATPase activity. The experiment was performed twice with similar results. **f**, ATPase activity of dimer and monomer fractions of WT and mutant MgtA purified in 5 mM $MgCl_2$. The assays were performed as described in Fig. 2c. Data are shown for duplicate experiments and mean. Data for WT MgtA are the same as in Fig. 2b,c.

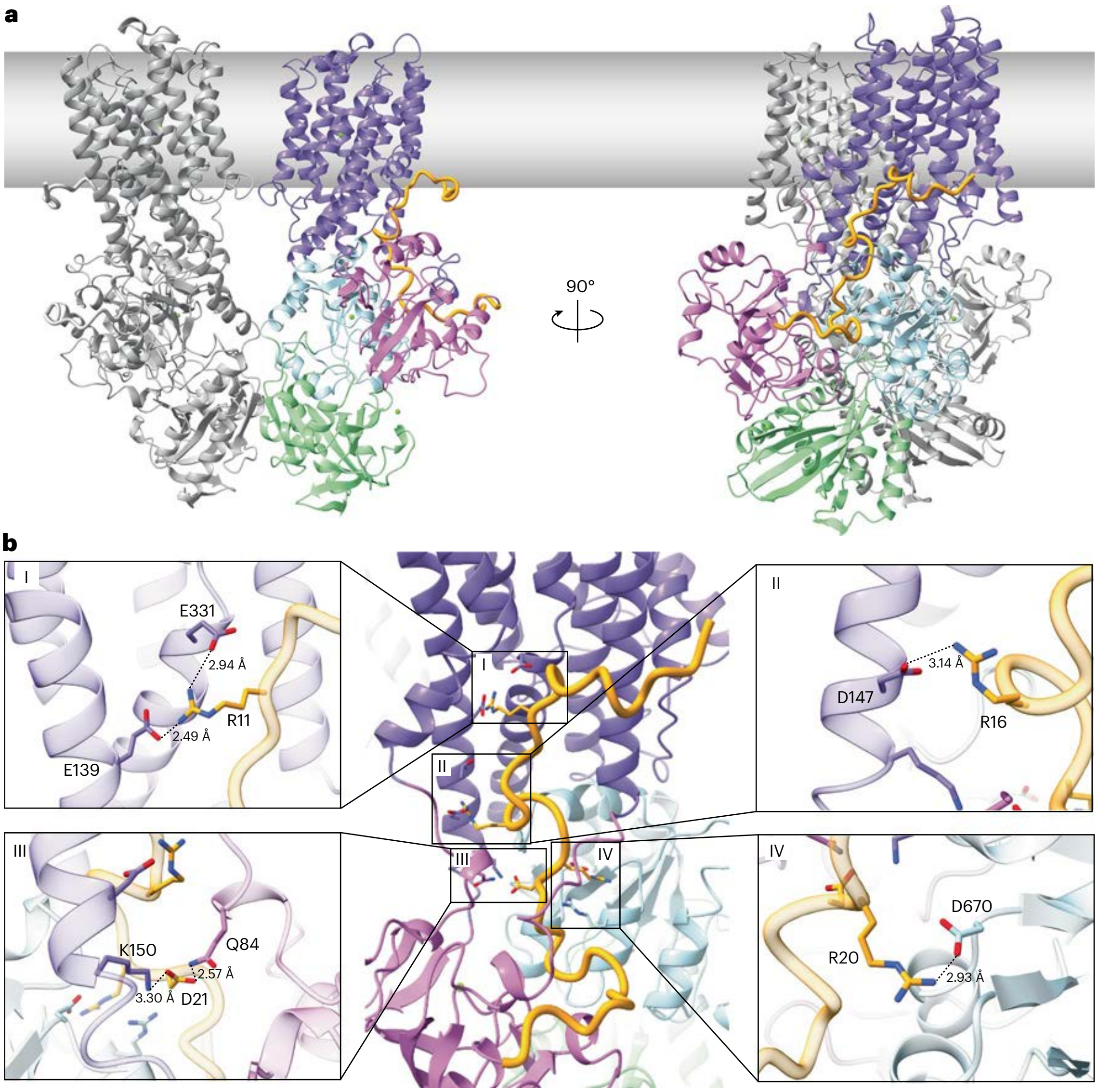

Fig. 5 | The extended N-terminus forms multidomain electrostatic interactions between the A, P and TM domains. a, Front and side views of the EcMgtA dimer structure with the left monomer in gray and the right monomer colored as in Fig. 1 with the N-terminus highlighted in a thicker orange loop. **b**, Close-up views of sites I–IV, which mark salt bridges formed between the N-terminus and the various domains of MgtA. All residues are represented in stick and colored by heteroatom.

N-terminal tail, which is found in some P-type ATPases and is not correctly predicted by AlphaFold. These data provide structural insights into the function of the MgtA family of bacterial Mg^{2+} importers and underscore the importance of mild extractions of membrane proteins to retain oligomeric states or complexes. Given the conservation among the P-type ATPase family of transporters, our work has implications for other members of this large protein family.

We performed structural comparisons between our structures, with those of closely related members of the 3A subfamily (PmaI) and more distantly related 2A subfamily (SERCA). This analysis revealed that the dimer most closely resembles an E1 or E1-ion bound state and the dimeric nucleotide-bound structure probably represents an E1-ATP state (Fig. 6a). The dimer was the major species upon GDN solubilization of membranes in 5 mM $MgCl_2$, and it is possible the resolved monomeric form of MgtA is only a product of dimer dissociation during protein purification. However, the monomer is structurally most similar to other P-type ATPases in their E2 state due to its more splayed cytosolic soluble domains as well as the conformational changes observed in TM1–4.

On the basis of what is known about other P-type ATPases, the MgtA importer is expected to bind Mg^{2+} from the periplasmic side in the E2P state. The Mg^{2+} is then expected to transition through the CBS and be released on the cytoplasmic side in the E1 state. We also expect there to be a counter ion that is exported from the cell analogous to what is known for SERCA Ca^{2+} pumps (Fig. 6a). This raises the questions of why we detected a Mg^{2+} ion in the membrane domain of the E1-like dimer and why this ion was not in the CBS. Additionally, why are there no obvious openings to either side of the membrane in any of the structures and only transient openings to the cytoplasm during MD simulations? It is possible that we have captured an intermediate step of transport. Alternatively, since many members of the P-type ATPases can be inhibited and the Mg^{2+} bound to site A is distant from the CBS, the monomeric and dimeric states may represent inhibited off-shoots of the normal post-Albers cycle, though we did not observe inhibition of ATP hydrolysis at the $MgCl_2$ concentration used for the cryo-EM samples. D780 is located in an ion-binding region of the TM that shares positional similarities to Na^+/K^+-ATPases Na^+-binding site III, which allows for sequential/cooperative binding of the additional cations[30].

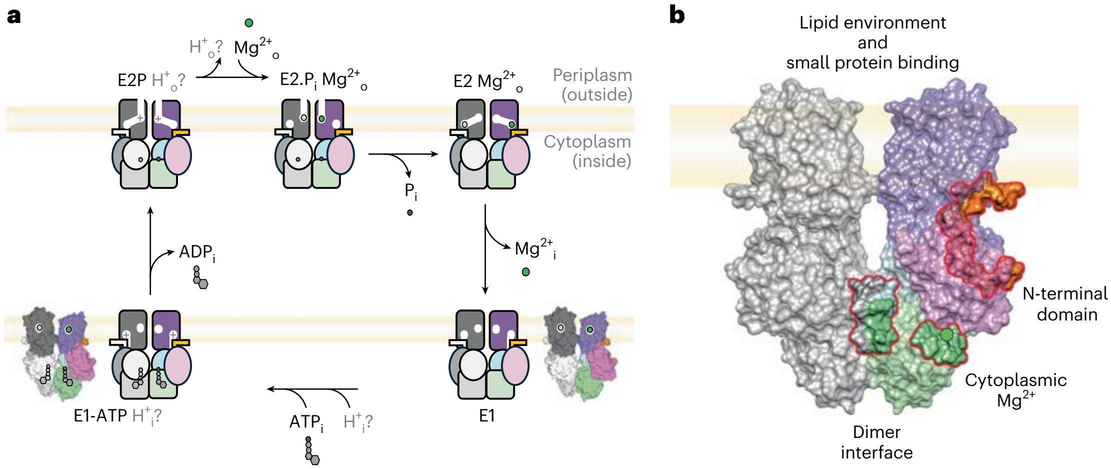

Fig. 6 | Summary of MgtA structural insights. a, Post-Albers cycle with proposed states of an MgtA dimer model based on known states from other P-type ATPases. Given that MgtA transports Mg^{2+} from the periplasm into the cytoplasm, a counter ion may be needed to complete the transport cycle. These states associate with a cytoplasmic ion-dependent autophosphorylation and periplasmic ion-dependent dephosphorylation, respectively. In the E1 state, P-type ATPases adopt a cytoplasmic side-open conformation where the ion-binding sites are open to the cytoplasm, allowing the cytoplasmic ion to access the transmembrane binding sites. Upon Mg-ATP and ion binding, P-type ATPases undergo autophosphorylation at the conserved aspartate residue in the P subdomain, thereby switching to an ion-occluded E1.P-ADP state where the ion-binding sites are not accessible to the cytoplasm. Upon ADP release, the P-type ATPases switch to an E2P state and the ion-binding sites open to the periplasmic side for ion release and subsequent periplasmic ion binding. The binding of the periplasmic ion triggers dephosphorylation and drives the conformational change of the P-type ATPase to an ion-occluded state (E2.P_i). The P-type ATPase subsequently switches to the E2 state after the release of the phosphate, and finally back to an E1 state releasing the ion into the cytoplasm allowing for the transport cycle to begin again. **b**, An overview of putative regulatory features of MgtA including the dimer interface, cytoplasmic Mg^{2+}-binding sites, N-terminal domain, lipid environment and small protein binding. Green circles represent Mg^{2+} ions. The color scheme is the same as in Fig. 1.

In several P-type ATPases, ion transport and ATP hydrolysis are coupled, and mutation of ion-binding sites reduces ATP hydrolysis[31,32]. The MgtA D780A mutant retained high ATPase activity in vitro, suggesting ion transport may be uncoupled from ATP hydrolysis. However, given the strong growth deficiency, the D780 site may be regulatory and required to facilitate the transport cycle. Additional structures and functional analysis are needed to gain further insights into the Mg^{2+} transport cycle and its regulation.

We suggest the two Mg^{2+} ion densities detected between the A domain and N or P subdomains in our dimeric MgtA structure have regulatory roles (Fig. 6b). The strong reduction in transport and ATPase activity for the D441A mutant and the proximity of D441 to F445, which forms interactions with ATP, indicates site C is important for regulating ATP binding and/or hydrolysis. The functional significance of site B will require additional probing since no defects were observed after mutating a limited number of surrounding residues.

Regulation also might be provided by dimerization, which could allow for functional coupling of the two monomer subunits in a concerted effort to reduce the overall activation energy required for the rate-limiting steps in the ion transport cycle (Fig. 6). This model is plausible given that the ATP-binding pocket of the dimer is accessible to nucleotides and that dimer-containing fractions of the protein have slightly higher ATP hydrolysis rates than monomer-containing fractions. Furthermore, enzyme coupling has previously been shown in other family members of the P-type ATPases such as the H^+-ATPase, Na^+/K^+-ATPase and the SERCA Ca^{2+}-ATPase[25,33,34]. Alternatively, our dimeric structure might only represent one state of the transport cycle, or oligomerization might regulate the stability of the protein. We suggest other members of the P-type ATPase subfamily 3B including *S. enterica* MgtB also form stable oligomers. A hexameric structure of the fungal H^+-transporter PmaI has already been solved[25]. Early studies of the SERCA Ca^{2+} transporter also showed that SERCA can oligomerize, dependent on detergents and lipid membrane composition[35–43]. Furthermore, recent work on the SERCA pump suggests that dimerization takes place in vivo[44] and is required for function[33,45], and the plasma membrane calcium ATPases have been reported to be regulated by dimerization[46]. It is increasingly evident that oligomerization of P-type ATPases should not be overlooked and warrants further studies.

The N-terminal tail of MgtA similarly may have a regulatory role (Fig. 6b). We observe that the putative ion-binding residue E331 contained within TM4 and the CBS is rotated outward toward the N-terminal tail in the dimeric structure and remains in close proximity during the entire 2 μs MD simulation. In the monomeric structure, TM4 unwinds and residue E331 appears to rotate toward TM α-helices 1, 2 and 6, presumably making it more accessible to ion binding. The A domain appears to be highly flexible in the monomeric form, and we were unable to resolve the N-terminus in this structure. We suggest that, in the dimer, the N-terminus regulates the translocation of ions across the membrane by preventing E331 from interacting with Mg^{2+} and restricting the large-scale rearrangements of the A domain and TM1–4 observed in the monomer. Consistent with these observations, our ATPase assays showed that truncation of the N-terminus reduced Mg^{2+} inhibition of ATPase activity, but did not abolish dimerization. A comparable regulatory role of the N-terminus could be extrapolated to fungal and plant H^+ pumps and the more distantly related Na^+/K^+-ATPases and H^+/K^+-ATPases, which possess equivalent extended N-termini.

One additional level of MgtA regulation already proposed by others is the lipid environment[16]. Given that P-type ATPases have been shown to be sensitive to detergents used for solubilization[38] and that they can respond to lipids such as cardiolipin, these transporters need to be characterized in their native lipid environments to further elucidate the impacts of oligomerization and lipid composition. Finally, small proteins of <50 amino acid in length control FtsH-mediated degradation of MgtA in both *E. coli* and *S. enterica*[8,21]. FtsH substrate recognition and degradation is sensitive to the oligomeric state of some substrates[47], but whether MgtA oligomerization is controlled by small proteins and whether dimerization affects degradation by FtsH are open questions. AlphaFold multimer analysis suggests that the small proteins share a common binding site on MgtA (Extended Data Fig. 10). However, the predicted binding site differs from a common interface bound by multiple small proteins, including Sarcolipin (SLN), Myoregulin (MLN), Phospholamban (PLN) and DWORF, that regulate the SERCA Ca^{2+} transporter[48–51] and from the site bound by the small KdpF subunit of the bacterial KdpFABC K^+ importer[52–54] and the FXYD subunit of the Na^+/K^+ pump[55,56] (Extended Data Fig. 10).

Future biochemical and structural studies of Mg^{2+} transporters will provide further mechanistic understanding of the unique MgtA features described here. This understanding, in turn, could provide insight into other P-type ATPases and ultimately aid in the design of therapeutic approaches targeted at this disease-relevant family of transporters.

Online content

Any methods, additional references, Nature Portfolio reporting summaries, source data, extended data, supplementary information, acknowledgements, peer review information; details of author contributions and competing interests; and statements of data and code availability are available at https://doi.org/10.1038/s41594-025-01593-7.

References

1. Moomaw, A. S. & Maguire, M. E. The unique nature of Mg^{2+} channels. *Physiology* **23**, 275–285 (2008).
2. Franken, G. A. C., Huynen, M. A., Martínez-Cruz, L. A., Bindels, R. J. M. & de Baaij, J. H. F. Structural and functional comparison of magnesium transporters throughout evolution. *Cell. Mol. Life Sci.* **79**, 418 (2022).
3. Jin, F., Huang, Y. & Hattori, M. Recent advances in the structural biology of Mg^{2+} channels and transporters. *J. Mol. Biol.* **434**, 167729 (2022).
4. Groisman, E. A., Duprey, A. & Choi, J. How the PhoP/PhoQ system controls virulence and Mg^{2+} homeostasis: lessons in signal transduction, pathogenesis, physiology, and evolution. *Microbiol. Mol. Biol. Rev.* **85**, e00176–00120 (2021).
5. Cunrath, O. & Bumann, D. Host resistance factor SLC11A1 restricts *Salmonella* growth through magnesium deprivation. *Science* **366**, 995–999 (2019).
6. Neef, J., Andisi, V. F., Kim, K. S., Kuipers, O. P. & Bijlsma, J. J. E. Deletion of a cation transporter promotes lysis in *Streptococcus pneumoniae*. *Infect. Immun.* **79**, 2314–2323 (2011).
7. Park, S.-Y. & Groisman, E. A. Signal-specific temporal response by the *Salmonella* PhoP/PhoQ regulatory system. *Mol. Microbiol.* **91**, 135–144 (2014).
8. Yeom, J., Shao, Y. & Groisman, E. A. Small proteins regulate *Salmonella* survival inside macrophages by controlling degradation of a magnesium transporter. *Proc. Natl Acad. Sci. USA* **117**, 20235–20243 (2020).
9. Hattori, M. et al. Mg^{2+}-dependent gating of bacterial MgtE channel underlies Mg^{2+} homeostasis. *EMBO J.* **28**, 3602–3612 (2009).
10. Dyla, M., Kjærgaard, M., Poulsen, H. & Nissen, P. Structure and mechanism of P-type ATPase ion pumps. *Annu. Rev. Biochem.* **89**, 583–603 (2020).
11. Jumper, J. et al. Highly accurate protein structure prediction with AlphaFold. *Nature* **596**, 583–589 (2021).
12. Varadi, M. et al. AlphaFold Protein Structure Database: massively expanding the structural coverage of protein-sequence space with high-accuracy models. *Nucleic Acids Res.* **50**, D439–D444 (2022).
13. Albers, R. W. Biochemical aspects of active transport. *Annu. Rev. Biochem.* **36**, 727–756 (1967).
14. Post, R. L. Seeds of sodium, potassium ATPase. *Annu. Rev. Physiol.* **51**, 1–15 (1989).
15. Lutsenko, S. & Kaplan, J. H. Organization of P-type ATPases: significance of structural diversity. *Biochemistry* **34**, 15607–15613 (1995).
16. Subramani, S., Perdreau-Dahl, H. & Morth, J. P. The magnesium transporter A is activated by cardiolipin and is highly sensitive to free magnesium in vitro. *eLife* **5**, e11407 (2016).
17. Møller, J. V., Olesen, C., Winther, A.-M. L. & Nissen, P. The sarcoplasmic Ca^{2+}-ATPase: design of a perfect chemi-osmotic pump. *Q. Rev. Biophys.* **43**, 501–566 (2010).
18. Aguayo-Ortiz, R. & Espinoza-Fonseca, L. M. Linking biochemical and structural states of SERCA: achievements, challenges, and new opportunities. *Int. J. Mol. Sci.* **21**, 4146 (2020).
19. Håkansson, K. O. The structure of Mg-ATPase nucleotide-binding domain at 1.6 Å resolution reveals a unique ATP-binding motif. *Acta Crystallogr. D* **65**, 1181–1186 (2009).
20. Burroughs, A. M., Allen, K. N., Dunaway-Mariano, D. & Aravind, L. Evolutionary genomics of the HAD superfamily: understanding the structural adaptations and catalytic diversity in a superfamily of phosphoesterases and allied enzymes. *J. Mol. Biol.* **361**, 1003–1034 (2006).
21. Wang, H. et al. Increasing intracellular magnesium levels with the 31-amino acid MgtS protein. *Proc. Natl Acad. Sci. USA* **114**, 5689–5694 (2017).
22. Bublitz, M. et al. Ion pathways in the sarcoplasmic reticulum Ca^{2+}-ATPase. *J. Biol. Chem.* **288**, 10759–10765 (2013).
23. Takahashi, M., Kondou, Y. & Toyoshima, C. Interdomain communication in calcium pump as revealed in the crystal structures with transmembrane inhibitors. *Proc. Natl Acad. Sci. USA* **104**, 5800–5805 (2007).
24. Winther, A. M. L. et al. Critical roles of hydrophobicity and orientation of side chains for inactivation of sarcoplasmic reticulum Ca^{2+}-ATPase with thapsigargin and thapsigargin analogs. *J. Biol. Chem.* **285**, 28883–28892 (2010).
25. Heit, S. et al. Structure of the hexameric fungal plasma membrane proton pump in its autoinhibited state. *Sci. Adv.* **7**, eabj5255 (2021).
26. Focht, D., Croll, T.I., Pedersen, B.P. & Nissen, P. Improved model of proton pump crystal structure obtained by interactive molecular dynamics flexible fitting expands the mechanistic model for proton translocation in P-type ATPases. *Front. Physiol.* **8**, 202 (2017).
27. Chen, Z. et al. Cryo-EM structures of human SPCA1a reveal the mechanism of Ca^{2+}/Mn^{2+} transport into the Golgi apparatus. *Sci. Adv.* **9**, eadd9742 (2023).
28. Diaz, D. & Clarke, R. J. Evolutionary analysis of the lysine-rich N-terminal cytoplasmic domains of the gastric H^+,K^+-ATPase and the Na^+,K^+-ATPase. *J. Membr. Biol.* **251**, 653–666 (2018).
29. Jephthah, S., Månsson, L. K., Belić, D., Morth, J. P. & Skepö, M. Physicochemical characterisation of KEIF—the intrinsically disordered N-terminal region of magnesium transporter A. *Biomolecules* **10**, 623 (2020).
30. Kanai, R., Ogawa, H., Vilsen, B., Cornelius, F. & Toyoshima, C. Crystal structure of a Na^+-bound Na^+,K^+-ATPase preceding the E1P state. *Nature* **502**, 201–206 (2013).
31. Zhang, Z. et al. Detailed characterization of the cooperative mechanism of Ca^2+ binding and catalytic activation in the Ca^{2+} transport (SERCA) ATPase. *Biochemistry* **39**, 8758–8767 (2000).
32. Nielsen, J. M., Pedersen, P. A., Karlish, S. J. & Jorgensen, P. L. Importance of intramembrane carboxylic acids for occlusion of K^+ ions at equilibrium in renal Na,K-ATPase. *Biochemistry* **37**, 1961–1968 (1998).
33. Bovo, E. et al. Dimerization of SERCA2a enhances transport rate and improves energetic efficiency in living cells. *Biophys. J.* **119**, 1456–1465 (2020).
34. Clarke, R. J. & Kane, D. J. Two gears of pumping by the sodium pump. *Biophys. J.* **93**, 4187–4196 (2007).
35. Dean, W. L. & Tanford, C. Reactivation of lipid-depleted Ca^{2+}-ATPase by a nonionic detergent. *J. Biol. Chem.* **252**, 3551–3553 (1977).
36. Hidalgo, C., Thomas, D. D. & Ikemoto, N. Effect of the lipid environment on protein motion and enzymatic activity of sarcoplasmic reticulum calcium ATPase. *J. Biol. Chem.* **253**, 6879–6887 (1978).

37. Jilka, R. L., Martonosi, A. N. & Tillack, T. W. Effect of the purified (Mg^{2+} + Ca^{2+})-activated ATPase of sarcoplasmic reticulum upon the passive Ca^{2+} permeability and ultrastructure of phospholipid vesicles. *J. Biol. Chem.* **250**, 7511–7524 (1975).
38. Maire, M. L., Lind, K. E., Jørgensen, K. E., Røigaard, H. & Møller, J. V. Enzymatically active Ca^{2+} ATPase from sarcoplasmic reticulum membranes, solubilized by nonionic detergents. Role of lipid for aggregation of the protein. *J. Biol. Chem.* **253**, 7051–7060 (1978).
39. Møller, J. V., Lind, K. E. & Andersen, J. P. Enzyme kinetics and substrate stabilization of detergent-solubilized and membraneous (Ca^{2+} + Mg^{2+})-activated ATPase from sarcoplasmic reticulum. Effect of protein–protein interactions. *J. Biol. Chem.* **255**, 1912–1920 (1980).
40. Taylor, K., Dux, L. & Martonosi, A. Structure of the vanadate-induced crystals of sarcoplasmic reticulum Ca^{2+}-ATPase. *J. Mol. Biol.* **174**, 193–204 (1984).
41. Vanderkooi, J. M., Ierokomas, A., Nakamura, H. & Martonosi, A. Fluorescence energy transfer between Ca^{2+} transport ATPase molecules in artificial membranes. *Biochemistry* **16**, 1262–1267 (1977).
42. Maire, M. L., Moller, J. V. & Tanford, C. Retention of enzyme activity by detergent-solubilized sarcoplasmic Ca^{2+}-ATPase. *Biochemistry* **15**, 2336–2342 (1976).
43. Toyoshima, C., Sasabe, H. & Stokes, D. L. Three-dimensional cryo-electron microscopy of the calcium ion pump in the sarcoplasmic reticulum membrane. *Nature* **362**, 467–471 (1993).
44. Blackwell, D. J., Zak, T. J. & Robia, S. L. Cardiac calcium ATPase dimerization measured by cross-linking and fluorescence energy transfer. *Biophys. J.* **111**, 1192–1202 (2016).
45. Ushimaru, M. & Fukushima, Y. The dimeric form of Ca^{2+}-ATPase is involved in Ca^{2+} transport in the sarcoplasmic reticulum. *Biophys. J.* **414**, 357–361 (2008).
46. Calì, T., Brini, M. & Carafoli, E. Regulation of cell calcium and role of plasma membrane calcium ATPases. *Int. Rev. Cell. Mol. Biol.* **332**, 259–296 (2017).
47. Hari, S. B., Morehouse, J. P., Baker, T. A. & Sauer, R. T. FtsH degrades kinetically stable dimers of cyclopropane fatty acid synthase via an internal degron. *Mol. Microbiol.* **119**, 101–111 (2022).
48. Akin, B. L., Hurley, T. D., Chen, Z. & Jones, L. R. The structural basis for phospholamban inhibition of the calcium pump in sarcoplasmic reticulum. *J. Biol. Chem.* **288**, 30181–30191 (2013).
49. Winther, A.-M. L. et al. The sarcolipin-bound calcium pump stabilizes calcium sites exposed to the cytoplasm. *Nature* **495**, 265–269 (2013).
50. Anderson, D. M. et al. A micropeptide encoded by a putative long noncoding RNA regulates muscle performance. *Cell* **160**, 595–606 (2015).
51. Nelson, B. R. et al. A peptide encoded by a transcript annotated as long noncoding RNA enhances SERCA activity in muscle. *Science* **351**, 271–275 (2016).
52. Silberberg, J. M. et al. Inhibited KdpFABC transitions into an E1 off-cycle state. *eLife* **11**, e80988 (2022).
53. Huang, C.-S., Pedersen, B. P. & Stokes, D. L. Crystal structure of the potassium-importing KdpFABC membrane complex. *Nature* **546**, 681–685 (2017).
54. Stock, C. et al. Cryo-EM structures of KdpFABC suggest a K^+ transport mechanism via two inter-subunit half-channels. *Nat. Commun.* **9**, 4971 (2018).
55. Morth, J. P. et al. Crystal structure of the sodium–potassium pump. *Nature* **450**, 1043–1049 (2007).
56. Shinoda, T., Ogawa, H., Cornelius, F. & Toyoshima, C. Crystal structure of the sodium–potassium pump at 2.4 Å resolution. *Nature* **459**, 446–450 (2009).
57. Laskowski, R. A. & Swindells, M. B. LigPlot+: multiple ligand-protein interaction diagrams for drug discovery. *J. Chem. Inf. Model.* **51**, 2778–2786 (2011).
58. Storz, G. Zeinert, R. Sodt, A. & Matthies, D. P-type ATPase magnesium transporter MgtA acts as a dimer. *figshare* https://doi.org/10.6084/m9.figshare.26820568.v1 (2025).
59. Toyoshima, C., Nomura, H. & Tsuda, T. Lumenal gating mechanism revealed in calcium pump crystal structures with phosphate analogues. *Nature* **432**, 361–368 (2004).
60. Nyblom, M. et al. Crystal structure of Na^+, K^+-ATPase in the Na^+-bound state. *Science* **342**, 123–127 (2013).

Methods

Plasmid and strain construction

All primers, plasmids and strains used in protein expression, complementation studies and co-immunoprecipitation studies can be found in Supplementary Tables 4–6, respectively. The pGEX-MgtA, pGEX-empty, pGEX-MgtA D373N, pGEX-MgtA E331A, pGEX-MgtA D738A, pGEX-MgtA D780A and pGEX-MgtA dimer (12-mer) plasmids were de novo gene synthesized by GenScript. Plasmids created in this study were assembled using the Gibson Assembly Cloning Kit (New England Biolabs). All plasmid sequences were confirmed by whole plasmid sequences services provided my Plasmidsaurus Inc.

Protein expression and membrane preparation

E. coli C43 (DE3) (Sigma, CMC0019) cells were transformed with the following plasmids pETDuet-1-MgtAS, pETDuet-1-MgtA, pETDuet-1-MgtA$_{D373N}$, pETDuet-1-MgtA$_{D780A}$, pETDuet-1-MgtA$_{D441A}$ or pETDuet-1-MgtA$_{\Delta 1-31}$ and allowed to recover for 1 h at 37 °C with shaking at 250 rpm. Following recovery, the cells were grown overnight at 37 °C with shaking in Luria-Bertani (LB) media containing 100 μg ml^{-1} ampicillin (amp) (GoldBIO). The saturated cultures were diluted 1:100 into LB media with 100 μg ml^{-1} amp and incubated at 37 °C to OD$_{600}$ ~0.2. The 2 l cultures were cooled to 18 °C before induction with 0.5 mM IPTG (GoldBIO) and then grown overnight at 18 °C shaking at 170–200 rpm. Cells were collected after 16 h by centrifugation at 5,000*g* for 10 min at 4 °C. As indicated in the text and figures, the following buffers were supplemented with either 0.5 or 5 mM MgCl$_2$. Cell pellets were resuspended in 50 mM Tris/HCl pH 7.5, 50 mM K$_2$SO$_4$, 1 mM dithiothreitol (DTT) (wash buffer), Roche cOmplete Protease Inhibitor Cocktail (Sigma) and 5% glycerol (for ATPase assays). The cell resuspension was passed through a microfluidizer processor (Microfluidics) at 20,000 psi three times. Crude cell lysate was cleared by centrifugation at 15,000*g* for 30 min. The cleared supernatant was centrifuged at 100,000*g* for 1 h. The membrane pellet was rinsed or washed by homogenization in 50 ml with wash buffer to remove residual soluble proteins. Membranes were resuspended using a Potter–Elvehjem-type tissue homogenizer at a final concentration of 10 mg ml^{-1}. All cell lysis steps were carried out at 4 °C. Glycerol was added to resuspended membranes at a final concentration of 20%. Aliquots were flash frozen in liquid nitrogen and stored at −80 °C until further use.

Optimization of membrane solubilization

Membranes (4–10 mg ml^{-1}) were solubilized with 1% GDN (Anatrace), a synthetic drop-in substitute for digitonin, 1% DDM (Sigma) or 1% LMNG (Anatrace) for 16 h rotating at 4 °C. Insoluble membranes were pelleted by centrifugation at 100,000*g* for 1 h at 4 °C. The supernatant containing detergent solubilized membrane proteins were then normalized for protein concentration, analyzed by native PAGE using 4–16% BisTris polyacylamide gels (blue native PAGE was used throughout). For native PAGE, samples were run 1 h at 150 V, followed by an additional 1 h at 250 V on ice. To allow for efficient transfer to PVDF membranes, the cathode buffer was replaced with diluted 1/10 (light blue) buffer when the protein had migrated 1/3 of the gel. The gels were then transferred to PVDF membranes for 1 h at 100 V. To mark the protein ladder, the membranes were stained with Ponceau S. Following Ponceau S staining, the blots were blocked with Tris-buffered saline with 0.1% Tween-20 detergent (TBST) + 5% milk and probed using TBST + 5% milk with anti-Flag (anti-Flag(R) M2-peroxidase (horseradish peroxidase (HRP)) (Sigma) or anti-His$_{6X}$ (His–HRP conjugate) (Qiagen) antibodies at a 1:1,000 dilution. Blots were washed three times with TBST for 5 min and imaged.

Protein purification

Membranes (10 mg ml^{-1}) were solubilized with 1% GDN for 16 h rotating at 4 °C. Insoluble membranes were pelleted by centrifugation at 100,000*g* for 1 h at 4 °C. Imidazole was added to the solubilized membrane proteins at a final concentration of 10 mM and the sample was batch bound with Ni-NTA resin for 3 h at 4 °C. For ATPase assays, 5% glycerol was added to the following buffers. Resin was washed with 30 column volumes of buffer A (50 mM Tris/HCl pH 7.5, 50 mM K$_2$SO$_4$, 0.5 or 5 mM MgCl$_2$, 10 mM imidazole, 0.007% GDN and 1 mM DTT). MgtA was eluted from Ni-NTA resin with buffer B (50 mM Tris/HCl pH 7.5, 50 mM K$_2$SO$_4$, 0.5 or 5 mM MgCl$_2$, 200 mM imidazole, 0.007% GDN and 1 mM DTT). Eluted MgtA was spin concentrated to ~15 mg ml^{-1} using 100 kDa Amicon centrifuge tubes. Then concentrated MgtA was spun at 15,000*g* for 30 min at 4 °C to remove aggregates before size exclusion chromatography (SEC) using a Superose 6 Increase 10/300 GL with buffer C (50 mM Tris/HCl pH 7.5, 50 mM K$_2$SO$_4$, 0.5 or 5 mM MgCl$_2$, 0.007% GDN and 2 mM DTT). Fractions were analyzed by SDS–PAGE and blue native PAGE using 4–16% BisTris polyacrylamide gels. For SDS–PAGE, samples were run at 200 V in Tris–glycine SDS buffer on ice until the dye front reached the bottom of the gel. For native PAGE, samples were run 1 h at 150 V, followed by an additional 1 h at 250 V on ice using cold buffer. The desired fractions were pooled, and spin concentrated using 100 kDa Amicon centrifuge tubes to ~2–3 mg ml^{-1} before cryo grid preparations.

ATP hydrolysis assay

MgtA was purified as described above with slight modifications. All buffers were supplemented with 5% glycerol and aliquots after SEC were flash frozen in liquid nitrogen before storage at −80 °C. MgtA ATPase assays for WT, D373N, D441A, D780A and Δ1–31 were performed at 37 °C in 50 mM Tris/HCl pH 7.5, 50 mM K$_2$SO$_4$, 5 mM MgCl$_2$ (unless otherwise indicated), 0.007% GDN, 2 mM DTT and 5% glycerol. As previously described[16], buffers were supplemented with 0.25 mM Na$_2$MoO$_4$, 5 mM NaN$_3$ and 20 mM KNO$_3$ to inhibit any contaminating F-type ATPases, phosphatases and pyrophosphatases. MgtA was used at 6.25 μg in a 200 μl reaction in the presence of 2 mM Na$^+$-ATP pH 7.5 with NaOH (Sigma, A2383-10G). The protein concentration was determined by Bradford protein assay according to the manufacturer's guidelines (Bio-Rad). Aliquots (20 μl) of the reactions were quenched with 20 μl of 500 mM EDTA at 1, 2, 3, 4, 5, 7.5 and 15 min time points. Free phosphate was measured using a modified Malachite green reagent (BIOMOL Green, Enzo) following the manufacturer's guidelines. Briefly, phosphate standards were made to calculate free phosphate. Reaction absorbances were measured at 620 nm and converted to phosphate based on standard curves using the phosphate standard. Linear regressions and slopes were measured from linear portions of the graph using GraphPad Prism (version 10.2.1). ATP turnover as a function of enzyme concentration were calculated by dividing the slopes by MgtA in milligrams to calculate ATP per min per mg. Enzymatic assays were performed in duplicate. Standard deviation and mean were calculated and graphs were plotted using GraphPad Prism.

Crosslinking and MS

MgtAS was purified as described above with slight modifications. To remove amines which interfere with crosslinking, HEPES was used in place of Tris. Purified MgtAS at a concentration of 1 mg ml^{-1} was crosslinked with 0.5% 1-ethyl-3-(3-dimethylaminopropyl)carbodiimide hydrochloride (Thermo Fisher Scientific) in 50 mM HEPES pH 7.5, 50 mM K$_2$SO$_4$, 5 mM MgCl$_2$, 0.007% GDN and 2 mM DTT at room temperature for 1 h. The protein samples were then quenched with equal volumes of 2× Laemmli loading buffer and heat-denatured at 95 °C for 5 min. Crosslinked MgtA was resolved using SDS–PAGE followed by Coomasie Blue G-250 staining. The ~100 kDa band for MgtA was cut and stored at −20 °C.

Gel bands were digested with the In-Gel Tryptic Digestion kit (Thermo Fisher Scientific) with minor adaptations. The excisions were destained, reduced and alkylated according to the manufacturer's protocol and digested overnight with trypsin (SERVA) followed by 4 h of digestions with chymotrypsin (Sigma-Aldrich) at 37 °C.

The digested peptides were transferred to a clean tube and solvents were evaporated in a speed vac (Eppendorf). Dried peptides were reconstituted in 5% acetonitrile (ACN) with 0.1% formic acid (FA). Peptides were loaded onto an Acclaim PepMap C_{18} capillary trapping column (particle size 3 µm, L = 20 mm) and separated on a ReproSil C_{18}-PepSep analytical column (particle size 1.9 µm, ID 75 µm, L = 50 cm, Bruker Corporation) using nano-high-performance liquid chromatography (Dionex U3000 RSLCnano) at a temperature of 55 °C. Trapping was carried out for 6 min with a flow rate of 6 µl min^{-1} using a loading buffer composed of 0.05% trifluoroacetic acid in H_2O. Peptides were separated by a gradient of water (buffer A: 100% H_2O and 0.1% FA) and ACN (buffer B: 80% ACN, 20% H_2O, and 0.1% FA) with a constant flow rate of 250 nl min^{-1}. The gradient went from 4% to 48% buffer B in 45 min. All solvents were liquid chromatography–mass spectrometry (LC–MS) grade and purchased from Riedel-de Häen/Honeywell (Seelze). Eluting peptides were analyzed in data-dependent acquisition mode on an Orbitrap Eclipse mass spectrometer (Thermo Fisher Scientific) coupled to nano-high-performance liquid chromatography by a Nano Flex ESI source. MS^1 survey scans were acquired over a scan range of 350–1,400 mass-to-charge ratio (m/z) in the Orbitrap detector (resolution 120k, automatic gain control $2e^5$ and maximum injection time 50 ms). Sequence information was acquired by a 'ddMS^2 OT HCD' MS^2 method with a fixed cycle time of 5 s for MS/MS scans. MS^2 scans were generated from the most abundant precursors with a minimum intensity of $5e^3$ and charge states from two to eight. Selected precursors were isolated in the quadrupole using a 1.4 Da window and fragmented using higher-energy C-trap dissociation at 30% normalized collision energy. For Orbitrap MS^2, an automatic gain control of $5e^4$ and a maximum injection time of 54 ms were used (resolution 30k). Dynamic exclusion was set to 30 s with a mass tolerance of 10 ppm. Each sample was measured in duplicate LC–MS/MS runs. MS raw data were processed using the MaxQuant software (version 2.1.0.0) with customized parameters for the Andromeda search engine. Spectra were matched to a FASTA file containing the MgtA (POABB8) and MgtS (A5A616) sequences downloaded from UniProtKB (April 2021), a contaminant and decoy database, with a minimum tryptic peptide length of six amino acids and a maximum of five missed cleavage sites. Precursor mass tolerance was set to 4.5 ppm and fragment ion tolerance to 20 ppm, with a static modification (carbamidomethylation) for cysteine residues. Acetylation on the protein N-terminus and oxidation of methionine residues were included as variable modifications. A false discovery rate below 1% was applied at crosslink, peptide and modification levels. Identified crosslinked peptides were manually curated and high-score crosslinks were mapped on a monomeric subunit of our dimeric MgtA cryo-EM structure (PDB 8UY7) using UCSF Chimera (version 1.18)[61], in which the distances between the sidechain of the residues was calculated.

HDX–MS

MgtAS was purified as previously described with slight modifications. For solubilization and purification the protein was initially solubilized from membranes using 1% DDM and the subsequent buffers were supplemented with 0.05% DDM. The final SEC buffer was adjusted to contain 5% glycerol as a cryo protectant and aliquots were flash frozen in liquid nitrogen before storage at −80 °C. Frozen samples were freshly thawed before every HDX–MS experiment. Equilibration (E) and labeling (L) buffers (50 mM Tris/HCl, 50 mM K_2SO_4, 5 mM $MgSO_4$, 2 mM DTT and 0.05% DDM, pH 7.5) with H_2O or D_2O, respectively, were equilibrated at 20 °C. Quench (Q) buffer (150 mM KPO_i and 0.05% DDM, pH 2.20) with H_2O was equilibrated at 0 °C. For ATP binding, L-buffer was split, one for a control and the other for the binding condition where we added 5 mM ATP (disodium salt, Sigma, A3377). Next, the sample was diluted from 17 µM to 15 µM with E-buffer containing no ATP and equilibrated at 0 °C. For ATPγS binding, we used the same buffers and conditions except 5 mM ATPγS (tetralithium salt, 119120-25MG) was added to the E- and L-buffers. Both samples (control and binding) were diluted with their respective E-buffers (without and with ATPγS) to a final concentration of 15 µM.

The HDX–MS experiments were carried out as described previously in ref. 62. In brief, the experiment was carried out using a fully automated HDX-2 system supplied by Waters. Protein samples were diluted in E-buffer for references measurements or L-buffer to start labeling for 2, 20, 60 and 120 min for the ATPγS experiment. In the ATP-binding experiment, the protein was labeled for 2 and 120 min. All time points were measured in quadruplicates. Next, the samples were quenched with ice-cold Q-buffer and immediately injected to the LC for online digestion with a Pepsin/Nepenthensin-2 column and C18 reverse phase peptide separation. Eluting peptides were measured on a Synapt-G2-Si mass spectrometer operated in HDMS^E mode including ion mobility separation for 3D peptide identification (room temperature, m/z, drift time).

Nondeuterated peptides were identified using ProteinLynx Global Server (version 3.0.3, Waters) for each condition (control and binding). Only peptides with a high confidence score (over 6) identified in at least three out of four replicates were retained for further HDX evaluation. Peak picking of all corresponding peaks was performed with HDExaminer software package by Sierra Analytics (version 3.0.3). All mass spectra of every peptide, time points and replicates were manually analyzed and curated for correct peak identification. Next, all peptides that displayed statistically significance deuterium uptake differences, based on a Student's t distribution with a 95% confidence interval ($P \leq 0.05$) in at least three out of four time points for ATPγS and all time points for ATP were used for further evaluation and visualization. Deuterium uptake difference maps created were plotted on our cryo-EM structures of MgtA (PDB 8UY7 (apo-dimer, C2) and 8UY9 (apo-monomer)) using UCSF Chimera[61].

Complementation assays

Function of MgtA and mutant alleles were assessed using a strain of *E. coli* lacking Mg^{2+} importers (BW25113 *ΔmgtA ΔcorA ΔyhiD DE*)[9]. Briefly, pGEX plasmids containing WT MgtA or mutants were transformed into the Mg^{2+}-auxotrophic strain with selection on plates supplemented with the appropriate antibiotics (50 µg ml^{-1} kanamycin (kan) or 100 µg ml^{-1} amp) and 100 mM $MgSO_4$ followed by growth at 37 °C overnight. Transformants were grown in LB supplemented with appropriate antibiotics and 100 mM $MgSO_4$ at 37 °C and 250 rpm shaking overnight. The overnight cultures were normalized to 0.1 OD_{600} and tenfold serially diluted before plating 3 µl of cells onto LB + agar (1.5% w/v) supplemented with antibiotics and either 100 mM, 1 mM or no additional $MgSO_4$. Cell samples were taken from overnight cultures, normalized by $OD_{600,}$ and immediately resuspended in 1× Laemmli loading buffer and stored at −20 °C before western blot analysis. For plated growth with induction, IPTG was added at 0.1 mM. Plates were incubated at 37 °C overnight before being imaged with a ChemiDoc MP Imaging System (Bio-Rad).

Immunoblot analysis

Frozen cell lysates were boiled at 95°C for 10 min 1× Laemmli loading buffer followed by centrifugation at 15,000g for 10 min to clear cellular debris. The resulting supernatant was run on precast 4–15% Tris–glycine gels (Bio-Rad, 4561086) at 200 V for 1 h. Proteins were transferred to nitrocellulose membranes at 100 V for 1 h. Following transfer, the blots were blocked with TBST + 5% milk and probed overnight at 4 °C using TBST + 5% milk with anti-MgtA (1:2,500; generated in this study). After overnight incubation, blots were washed three times with TBST for 5 min and probed with goat anti-rabbit HRP antibody (1:10,000) for 1 h at room temperature. Blots were washed three times with TBST for 5 min and visualized using a ChemiDoc MP Imaging System (Bio-Rad).

In vivo dimerization assay

BW25113 *ΔmgtA ΔcorA ΔyhiD DE* cells were transformed with the plasmids pBAD24-MgtA-H6 and pACYC-MgtA-SPA or pBAD-MgtA-H6 and empty pACYC vector, allowed to recover for 1 h at 37 °C with shaking at 250 rpm. Following transformation cells were plated onto LB + agar plates containing 100 µg ml^{-1} ampicillin and 50 µg ml^{-1} kan, and 100 mM $MgSO_4$ and grown at 37 °C overnight. Large culture overnights were inoculated with single colonies and grown overnight at 37 °C with shaking in LB media containing 100 µg ml^{-1} amp and 50 µg ml^{-1} kan. Cells were collected by centrifugation at 5,000*g* for 10 min at 4 °C. Cell pellets were resuspended in 50 mM Tris/HCl pH 7.5, 50 mM K_2SO_4, 5 mM $MgCl_2$ (wash buffer) and Roche cOmplete Protease Inhibitor Cocktail. Membranes were isolated as previously described for MgtAS purification and resuspended at a final concentration of 10 mg ml^{-1}.

Membranes (10 mg ml^{-1}) were solubilized with 1% GDN for 16 h rotating at 4 °C. Insoluble membranes were pelleted by centrifugation at 100,000*g* for 1 h at 4°C. The sample was batch bound with Flag resin for 2 h at 4 °C. Resin was washed with 30 column volumes of Buffer A (50 mM Tris/HCl pH 7.5, 50 mM K_2SO_4, 5 mM $MgCl_2$ and 0.007% GDN). MgtA was eluted from Flag resin with 0.2 M glycine pH 2.4 and neutralized in 1× Laemmli loading buffer. Elutions were analyzed by western blot using polyclonal anti-MgtA as described for the complementation assays.

Negative-staining EM

First, 3 µl diluted MgtA (0.01 mg ml^{-1}) was deposited on a carbon-coated 400 mesh copper grid (EMS, CF400-CU) following glow discharging (PELCO easiGlow Glow Discharge Cleaning System) for 1 min at 15 mA. The liquid drop was allowed to incubate on the grid for 1 min. The liquid was then wicked away with blotting paper (Whatman) and quickly washed with 3 µl of Nano-W Negative Stain (2% methylamine tungstate, Nanoprobes) followed by immediate incubation with 3 µl of Nano-W for one additional min. Filter paper was used to wick away excess stain, followed by gently waving the grid for 1 min to produce different thicknesses or waves of stained areas. Transmission electron microscopy (TEM) was performed using an FEI Tecnai T20 transmission electron microscope (Thermo Fisher) operated at a voltage of 200 kV with a direct electron detector K2 Summit (Gatan Inc.) using SerialEM (version 3.2)[63]. Data were collected at a nominal magnification of 25,000×, a binned pixel size of 3.04 Å px^{-1} and a defocus ranging from ~1.3 to ~2.4 µm. At a dose rate of 5 e^{-} px^{-1} s^{-1}, 10 s exposures with 0.2 s frames were collected. Each 50-frame movie was motion corrected using SerialEM[63], and a total of 343 images were collected. Data were unpacked using Bsoft[64] and processed in CisTEM (version 1.0.0)[65]. Aligned images were imported, contrast transfer function (CTF) was estimated and particles picked using a maximum radius of 90 Å and a characteristic radius of 30 Å and a threshold of 5. 76,993 particles were extracted using a box size of 84 px (~255 Å) and multiple rounds of 2D classification were performed.

Cryo-EM grid preparation

For apo-MgtA grids, Quantifoil R1.2/1.3 400 mesh copper grids (EMS, Q4100CR1.3) were glow discharged in a PELCO easiGlow Glow Discharge Cleaning System (PELCO easiGlow Glow Discharge Cleaning System) at 15 mA for 1 min. MgtAS sample (3 µl) at a concentration of 3.2 mg ml^{-1} (Extended Data Fig. 3b) was applied to the glow discharged grids. After blotting for 4–5 s in a Leica EM GP2 plunge freezer (Leica Microsystems) with the chamber set to 5 °C and 95% humidity, the grids were immediately plunge frozen into liquid ethane and stored in liquid nitrogen. Grids were initially screened on an FEI Tecnai T20 transmission electron microscope operated at a voltage of 200 kV with a direct electron detector K2 Summit using SerialEM[63].

For nucleotide–MgtA grids, Quantifoil R1.2/1.3 400 mesh copper grids were prepared as described above. Before grid preparations, MgtAS consisting of a predominantly dimer species was isolated using SEC and spin concentrated to a final concentration of 2.3 mg ml^{-1} (Extended Data Fig. 3c). After spin concentration, 10 µl of MgtAS was incubated with 0.5 µl of 100 mM ATP (disodium salt hydrate, Sigma, A2383-10G) (for 2 min), ATPγS (tetralithium salt, Sigma, 119120-25 mg) (for 15 min) or ADP (sodium salt, Sigma, A2754-1G) (for 15 min) and 3 µl were applied to the glow discharged grids. After blotting for 6 s using a Leica EM GP2 plunge freezer with the chamber kept at 4 °C and 95% humidity, the grids were immediately plunge frozen into liquid ethane and stored in liquid nitrogen.

Cryo-EM data collection

After the grid-making conditions were optimized, high-resolution movies were collected on a G1 or G4 Titan Krios electron microscope (Thermo Fisher) operated at 300 kV with a K3 direct electron detector in correlated double sampling mode and energy filter using a 20 eV slit (Gatan Inc.). The image acquisition was operated with SerialEM[63] at a nominal magnification of 105,000×, a physical pixel size of 0.83 (G1 Krios) or 0.85 (G4 Krios) Å px^{-1} in super-resolution mode (0.415 or 0.425 Å px^{-1}) and a defocus ranging from approximately −0.7 to −2.0 µm. A first dataset was collected with a dose rate of 9.5 Å px^{-1} s^{-1} (~7.5 on the camera through the sample), exposure time 0.0712 s per frame (~1 e^{-} Å^{-2}) and total exposure time of 4.31 s per movie (~60 e^{-} Å^{-2}), resulting in a total of 10,246 movies with 60 frames each. An additional six datasets were collected in a similar manner and the data collection details can be found in Supplementary Information.

Cryo-EM data processing

The overall workflow of image processing of *E. coli* MgtA is illustrated in and additional details can be found in Supplementary Information. All processing of MgtA without the addition of any nucleotides (datasets 1 and 2) was performed within cryoSPARC (version 3.2)[66]. Datasets 3–7 of MgtA in the presence of different nucleotides were processed using cisTEM (version 1.0.0)[65] and cryoSPARC[66].

For datasets 1 and 2, movies were processed with full-frame motion correction and patch CTF estimation. CryoSPARC's blob picker with a minimum and maximum particle diameter of 110 and 130 Å was used for automatic particle picking. Particles were extracted using a box size of 768 px (~319 Å), fourier cropped to 384 px. For datasets 1 and 2, 1,578,214 and 1,775,726 particles were picked from 10,164 and 5,778 selected aligned micrographs. Particles were then subjected to 2D classification to remove junk particles. Then, 1,068,828 and 725,244 particles selected from one round of 2D classification were subjected to a second round of 2D classification. At this point, particles from 2D class averages showing clear side views for dimer and monomer species were separated, while particles from less clear views including top and tilted views were added to both subsets. Ab initio reconstruction followed by nonuniform refinement led to initial dimer and monomer reconstructions that were used for heterogeneous refinement using all particles to include possible discarded particles during earlier classifications. Additional ab initio reconstructions followed by nonuniform refinement was used to cluster the best aligning particles and to improve resolution further, and local motion correction and CTF refinement to correct for beam tilt, spherical aberrations and per-particle defocus parameters was applied before merging dimer or monomer particles from the two different datasets. Final rounds of 2D classification, ab initio reconstruction, and nonuniform refinements were used to produce the final reconstructions that were used to estimate and filter to local resolution. All refinements of the dimer were run with (C2) and without (C1) symmetry, while all refinements of the monomer were performed without symmetry. The final dimer map was reconstructed from 160,139 particles to an average resolution of 2.93 Å (C2) or 3.03 Å (C1), while the final monomer map was reconstructed from 78,231 particles to an average resolution of 3.65 Å according to the gold-standard Fourier shell correlation (FSC) 0.143 criterion.

For datasets 3–7, movies were imported and binned to a pixel size of 0.83 (G1 Krios data, datasets 3–6) or 0.85 (G4 Krios, dataset 7), processed with full-frame motion correction and patch CTF estimation using CisTEM[65]. After image selection, particles were picked using a maximum radius of 70 Å, a characteristic radius of 50 Å and a threshold of 3. Particles were extracted using a box size of 384 px (~319 or ~326 Å) and one round of 2D classification was performed before only getting rid of particles in junk 2D class averages and exporting the selected particle stacks for further processing in cryoSPARC[66]. Additional rounds of 2D classification, ab initio reconstructions, nonuniform and heterogeneous refinements were performed before ending up with final maps at an average resolution of 3.72 Å, 3.87 Å and 3.75 Å for the MgtA dimer in the presence of 5 mM ATP, ATPγS and ADP, respectively.

Model building, refinement and validation

A preliminary structural model was generated using both an AlphaFold prediction (AF-P0ABB8) and the 1.6 Å crystal structure of the MgtA nucleotide-binding subdomain spanning residues 382–545 of the total of 898 residues (PDB 3GWI (ref. 67)). Using UCSF Chimera (version 1.18)[61], the AlphaFold model was separated into overlapping fragments (fragment 1, containing residues 1–86 and 149–281; fragment 2, containing residues 366–548; fragment 3, containing residues 540–700; fragment 4, containing residues 375–548; fragment 5, containing residues 86–144 for TM1–2; and fragment 6, containing residues 270–347 and 697–898 for TM3–4 and TM5–10) and rigid body docked into our 3D dimer map. Following docking, regions that did not fit including the N-terminal tail were removed and built manually followed by flexible fitting in Coot (version 0.8.9.3)[68]. In regions of the structure that were less clearly resolved, the local resolution filtered as well as the nonsharpened map were used to trace the backbone and to connect segments. Further refinement of the structures was performed using real-space refinement in PHENIX (version 1.20)[69]. The geometry of the structural model was additionally validated using MolProbity (version 4.02)[70]. UCSF Chimera and ChimeraX (version 1.8)[71] were used for visualization of the structures and to generate figures in the manuscript. Videos, not including MD simulations, were created using UCSF Chimera. The statistics for the model refinements are presented in Table 1 and Supplementary Tables 7 and 8. The fitted PDBs have been made available together with the EM maps with the following PDB IDs: 8UY7 (apo-dimer, C2), 8UY8 (apo-dimer, C1), 8UY9 (apo-monomer, C1), 8UYA (ATP-dimer, C2), 8UYB (ATPγS-dimer, C2) and 8UYC (ADP-dimer, C2).

MD simulations

Simulations were built with the CHARMM-GUI (version 3.7) web interface[72] using an early cryo-EM resolved dimer structure of MgtA with only the TM Mg^{2+} cation included. Symmetric bilayers were constructed with 16:0,18:1(Δ11)-phosphatidylglycerol (PVPG, 20%), 16:0,16:1(Δ9)-phosphatidylethanolamine (PPPE, 75%) and 16:0,18:1(Δ11),16:0,18:1(Δ11)-cardiolipin (PVCL2, 5%), mimicking the headgroup chemical composition of the *E. coli* inner membrane, if not the potential (dynamic) asymmetry[73]. The CHARMM C36m forcefield was used for proteins[74] and lipids[75]. Following initial equilibration and minimization with NAMD[76], production simulations were run with the Amber software package (Amber20 version 20.0). Temperature was maintained at 310 K using a Langevin thermostat. Constant atmospheric pressure and zero surface tension was maintained using a Monte Carlo semi-isotropic barostat. Standard CHARMM forcefield parameters were applied (Particle Mesh Ewald for electrostatics, a 12 Å cutoff for nonbonded interactions with force switching between 10 and 12 Å). Simulations of the early cryo-EM resolved MgtA dimer, the ATP-bound configuration and the monomer were run for 2, 1.8 and 2.3 total microseconds, respectively. Simulations of the dimer with K^+ substituted at site A were run for 800 ns. Enhanced sampling perturbing Mg^{2+}/ K^+ ions were computed in AMBER with the adaptive biasing MD module in flooding mode using a 100 ps time constant, applying biasing to the aspartic acid gamma carbon to Mg^{2+}/K^+ distance. Three replicas for each Mg^{2+} site, and one for K^+ in site A, were run for 440 ns each. Trajectories and AMBER input files for simulations with and without ATP are publicly available via Zenodo[77]. Water paths were identified using a 3.4 Å cutoff between water oxygens.

Lipid solvation shell composition is resolved by a Voronoi decomposition as in ref. 78. Five representative protein-bound ATP configurations were found via K-medoids[79] clustering on ~1,800 configurations. Lipid shell analysis[80] and ATP clustering[81] were performed with public-domain software developed in house.

Static molecular images from simulations were created using UCSF Chimera[61]. Simulation movies were created with Tachyon (version 0.98.9) (written by John Stone) and assembled with ffmpeg.

Sequence analysis

MgtA (National Center for Biotechnology Information (NCBI) Genbank database accession: NP_418663.1) was used as starting query for sequence similarity searches using PSI-BLAST program against the nonredundant clustered down to 50% sequence identity using the MMseqs program with a profile-inclusion threshold set at an e-value of 10^{-10}. Multiple sequence alignments were constructed using the MAFFT programs. Sequence logos were constructed using these alignments with the ggseqlogo library for the R language. Signal peptides and TM regions were predicted using hidden Markov model specifying different sequence regions of a signal peptide and TM proteins in series of interconnected states as implemented in the Phobius program.

Structure analysis

The JPred program was used to predict secondary structures using multiple sequence alignments (see above). Structural models were generated using the RoseTTAfold[82] and AlphaFold2 (ref. 11) programs. Multiple alignments of related sequences (>30% similarity) were used to initiate HHpred searches for the step of identifying templates to be used by the neural networks deployed by these programs.

Comparative genomics and phylogenetic analysis

Clustering of proteins was done using the MMseqs program adjusting the length of aligned regions and bit-score density threshold empirically. Divergent sequences or small clusters were merged with larger clusters if other lines of evidence, including shared sequence motifs, reciprocal BLAST search results and/or shared genome context associations, supported their inclusion. Phylogenetic analysis was performed using the maximum-likelihood method with the WAG or JTT models (determined empirically from data) with the IQTree (version 1.6.12). The FigTree program (version 1.4.4) (ref. 83) was used to render phylogenetic trees.

Statistics and reproducibility

Unless otherwise noted, experiments shown in all figures were repeated independently at least two times with similar consistent results.

Reporting summary

Further information on research design is available in the Nature Portfolio Reporting Summary linked to this article.

Data availability

Cryo-EM maps have been deposited in the Electron Microscopy Data Bank (EMDB) under accession codes EMD-42794 (apo-dimer, C2), EMD-42795 (apo-dimer, C1), EMD-42796 (apo-monomer, C1), EMD-42797 (ATP-dimer, C2), EMD-42798 (ATPγS-dimer, C2) and EMD-42799 (ADP-dimer, C2). The atomic coordinates have been deposited in the PDB under accession codes 8UY7 (apo-dimer, C2), 8UY8 (apo-dimer, C1), 8UY9 (apo-monomer, C1), 8UYA (ATP-dimer,

Table 1 | Cryo-EM data collection, refinement and validation statistics

	No. 1 MgtA, dimer (C2) (EMDB-42794) (PDB 8UY7)	No. 2 MgtA, dimer (C1) (EMDB-42795) (PDB 8UY8)	No. 3 MgtA, monomer (C1) (EMDB-42796) (PDB 8UY9)	No. 4 MgtA, dimer, with ATPγS (C2) (EMDB-42798) (PDB 8UYB)	No. 5 MgtA, dimer, with ADP (C2) (EMDB-42799) (PDB 8UYC)	No. 6 MgtA, dimer, with ATP (C2) (EMDB-42797) (PDB 8UYA)
Data collection and processing						
Magnification	105,000×	105,000×	105,000×	105,000×	105,000×	105,000×
Voltage (kV)	300	300	300	300	300	300
Electron exposure (e$^-$ Å^{-2})	50–60	50–60	50–60	50	50	50
Defocus range (μm)	−1 to −2	−1 to −2	−1 to −2	−0.7 to −1.8	−0.8 to −1.5	−0.8 to −1.8
Pixel size (Å)	0.83	0.83	0.83	0.83	0.83	0.85
Symmetry imposed	C2	C1	C1	C2	C2	C2
Initial particle images (no.)	3,353,940	3,353,940	3,353,940	1,783,325	1,456,447	2,339,956
Final particle images (no.)	160,139	160,139	78,231	28,120	28,666	48,080
Map resolution (Å)	2.93	3.03	3.65	3.87	3.75	3.72
FSC threshold	(FSC 0.143)	(FSC 0.143)	(FSC 0.143)	(FSC 0.143)	(FSC 0.143)	(FSC 0.143)
Map resolution range (Å)	1.9–3.3	2.0–3.7	2.3–8.0	2.5–5.0	2.5–4.5	2.5–4.0
Refinement						
Initial model used (PDB code)	AF-POABB8, 3GWI	MgtA dimer (C2)	MgtA dimer (C2)	MgtA dimer (C2)	MgtA dimer (C2)	MgtA dimer (C2)
Model resolution (Å)	3.0	3.1	3.7	3.9	3.8	3.7
FSC threshold	(FSC 0.5)	(FSC 0.5)	(FSC 0.5)	(FSC 0.5)	(FSC 0.5)	(FSC 0.5)
Map sharpening *B* factor (Å^2)	104	92	106	123	110	133
Model composition						
Nonhydrogen atoms	14,038	13,930	6,587	13,882	13,828	13,904
Protein residues	1,796	1,794	859	1,796	1,796	1,796
Ligands	6	6	1	8	6	10
B factors (Å^2)						
Protein	70.57	82.25	93.11	115.65	69	56.5
Ligand	62.47	73.88	53.08	113.7	58.8	46.6
Root mean squared deviations						
Bond lengths (Å)	0.003	0.003	0.003	0.002	0.002	0.002
Bond angles (°)	0.612	0.551	0.652	0.511	0.517	0.54
Validation						
MolProbity score	1.62	1.64	1.64	1.75	1.64	1.82
Clashscore	7.49	6.73	9.69	8.53	7.64	6.44
Poor rotamers (%)	0.06	0.00	0.00	0.00	0.00	0.00
Ramachandran plot						
Favored (%)	96.65	96.20	97.32	95.81	96.54	92.63
Allowed (%)	3.29	3.74	2.68	4.19	3.46	7.37
Disallowed (%)	0.06	0.06	0.00	0.00	0.00	0.00

C2), 8UYB (ATPγS-dimer, C2) and 8UYC (ADP-dimer, C2). Trajectories and AMBER input files for simulations with and without ATP are publicly available via Zenodo at https://doi.org/10.5281/zenodo.10017395 (ref. 77). The MS proteomics data have been deposited to the ProteomeXchange Consortium via the PRIDE partner repository[84] with the dataset identifier PXD047999. The MgtA (POABB8) and MgtS (A5A616) sequences can be readily downloaded from UniProtKB. Additional source data for Figs. 2–4 and Extended Data Fig. 2 are available via figshare at https://doi.org/10.6084/m9.figshare.26820568.v1 (ref. 58). All other data supporting the findings of this study are available from the corresponding authors on reasonable request. Source data are provided with this paper.

Code availability

Calculation of water pathway code is available via GitHub at https://github.com/alexsodt/WaterPathMGTA.

References

61. Pettersen, E. F. et al. UCSF Chimera—a visualization system for exploratory research and analysis. *J. Comput. Chem.* **25**, 1605–1612 (2004).
62. Zöller, J. et al. Ligand binding and conformational dynamics of the *E. coli* nicotinamide nucleotide transhydrogenase revealed by hydrogen/deuterium exchange mass spectrometry. *Comput. Struct. Biotechnol. J.* **20**, 5430–5439 (2022).

63. Mastronarde, D. N. Automated electron microscope tomography using robust prediction of specimen movements. *J. Struct. Biol.* **152**, 36–51 (2005).
64. Heymann, J. B. Guidelines for using Bsoft for high resolution reconstruction and validation of biomolecular structures from electron micrographs. *Protein Sci.* **27**, 159–171 (2018).
65. Grant, T., Rohou, A. & Grigorieff, N. *cis*TEM, user-friendly software for single-particle image processing. *eLife* **7**, e35383 (2018).
66. Punjani, A., Rubinstein, J. L., Fleet, D. J. & Brubaker, M. M. cryoSPARC: algorithms for rapid unsupervised cryo-EM structure determination. *Nat. Methods* **14**, 290–296 (2017).
67. Håkansson, K. O. The structure of Mg-ATPase nucleotide-binding domain at 1.6 Å resolution reveals a unique ATP-binding motif. *Acta Crystallogr. D* **65**, 1181–1186 (2009).
68. Emsley, P., Lohkamp, B., Scott, W. G. & Cowtan, K. Features and development of Coot. *Acta Crystallogr. D* **66**, 486–501 (2010).
69. Liebschner, D. et al. Macromolecular structure determination using X-rays, neutrons and electrons: recent developments in Phenix. *Acta Crystallogr. D* **75**, 861–877 (2019).
70. Williams, C. J. et al. MolProbity: more and better reference data for improved all-atom structure validation. *Protein Sci.* **27**, 293–315 (2018).
71. Goddard, T. D. et al. UCSF ChimeraX: meeting modern challenges in visualization and analysis. *Protein Sci.* **27**, 14–25 (2018).
72. Jo, S., Kim, T., Iyer, V. G. & Im, W. CHARMM-GUI: a web-based graphical user interface for CHARMM. *J. Comput. Chem.* **29**, 1859–1865 (2008).
73. Bogdanov, M. et al. Phospholipid distribution in the cytoplasmic membrane of Gram-negative bacteria is highly asymmetric, dynamic, and cell shape-dependent. *Sci. Adv.* **6**, eaaz6333 (2020).
74. Huang, J. et al. CHARMM36m: an improved force field for folded and intrinsically disordered proteins. *Nat. Methods* **14**, 71–73 (2017).
75. Klauda, J. B. et al. Update of the CHARMM all-atom additive force field for lipids: validation on six lipid types. *J. Phys. Chem. B* **114**, 7830–7843 (2010).
76. Phillips, J. C., Zheng, G., Kumar, S. & Kale, L. V. NAMD: biomolecular simulation on thousands of processors. In *Proc. 2002 ACM/IEEE Conference on Supercomputing* 36 (IEEE, 2002).
77. Sodt, A. & Lessen, H. Simulations of the bacterial magnesium transporter MgtA with and without bound ATP. *Zenodo* https://doi.org/10.5281/zenodo.10017395 (2025).
78. Beaven, A. H. et al. Gramicidin A channel formation induces local lipid redistribution I: experiment and simulation. *Biophys. J.* **112**, 1185–1197 (2017).
79. Kaufman, L. & Rousseeuw, P. J. in *Wiley Series in Probability and Statistics* Ch. 2, 68–125 (Wiley, 1990).
80. Sodt, A. Shells. *GitHub* http://github.com/alexsodt/shells (2025).
81. Sodt, A. Clustering. *GitHub* https://github.com/alexsodt/clustering (2025).
82. Baek, M. et al. Accurate prediction of protein structures and interactions using a three-track neural network. *Science* **373**, 871–876 (2021).
83. FigTree. *Molecular Evolution, Phylogenetics and Epidemiology* http://tree.bio.ed.ac.uk/software/figtree/ (2025).
84. Perez-Riverol, Y. et al. The PRIDE database resources in 2022: a hub for mass spectrometry-based proteomics evidences. *Nucleic Acids Res.* **50**, D543–D552 (2022).

Acknowledgements

We thank A. Banerjee for the use of his lab's AKTA and both A. Banerjee and M. Britt for comments on the paper; J. Petersen and J. Zimmerberg for access to the T20 electron microscope; the NICE facility with A. Zeher, Z. Lang and R.K. Huang for support on the G1 Krios electron microscope; E. Viverette, J. Bouvette and M. Borgnia for support on the G4 Krios electron microscope; and S. Mahé and J. Cometa for technical support on the T20 and G1 Krios. We also thank K. Ito for providing us the Mg^{2+}-auxotrophic *E. coli* strain (BW25113 Δ*mgtA*, Δ*corA*, Δ*yhiD* DE3). This research was supported by the Intramural Research Programs of the Eunice Kennedy Shriver National Institute of Child Health and Human Development (NICHD) (grant nos. ZIA HD008955 (to A.J.S.), ZIA HD008855 (to G.S.) and ZIA HD008998 (to D.M.)) and the National Library of Medicine (grant no. LM594244 (to L.A.)) as well as a NIGMS PRAT fellowship (grant no. 1FI2GM146628-01 (to R.Z.)) and NICHD Early Career Awards to R.Z. and D.M. and funding from the German Research Foundation (grant no. DFG 3542/1-1 (to J.D.L.)). This work utilized the computational resources of the NIH HPC Biowulf cluster (http://hpc.nih.gov).

Author contributions

R.Z. expressed and purified protein, performed SDS–PAGE and western blots, mutagenesis, in vivo assays and ATP hydrolysis; made negative-staining and cryo-EM grids; analyzed data, generated figures and wrote the paper. F.Z. performed native PAGE, made negative-staining and cryo-EM grids, screened negative-staining and cryo-EM grids, and helped collect negative-staining and cryo-EM data. P.F. performed MS analysis of crosslinked samples, data evaluation and generated figures. J.Z. performed HDX–MS experiments and HDX–MS data evaluation and generated figures. Z.K.M. expressed and purified protein, performed SDS–PAGE and western blots and ATP hydrolysis. H.L. performed MD simulations. L.A. carried out computation sequence/structural and evolutionary analysis, identified sequence motifs and generated the large sequence alignment. J.D.L. analyzed crosslinking and HDX–MS data. A.J.S. performed MD simulations, analyzed data, generated figures, wrote the paper and designed and supervised the project. G.S. analyzed data, generated figures, wrote the paper, initiated and designed and supervised the project. D.M. collected and processed negative-staining data, processed cryo-EM data, produced structural models, analyzed data, generated figures, wrote the paper and designed and supervised the project. All authors contributed to the paper.

Competing interests

The authors declare no competing interests.

Additional information

Extended data is available for this paper at https://doi.org/10.1038/s41594-025-01593-7.

Supplementary information The online version contains supplementary material available at https://doi.org/10.1038/s41594-025-01593-7.

Correspondence and requests for materials should be addressed to Alexander J. Sodt, Gisela Storz or Doreen Matthies.

Peer review information *Nature Structural & Molecular Biology* thanks Kazuhiro Abe and the other, anonymous, reviewer(s) for their contribution to the peer review of this work. Peer reviewer reports are available. Primary Handling Editor: Katarzyna Ciazynska, in collaboration with the *Nature Structural & Molecular Biology* team.

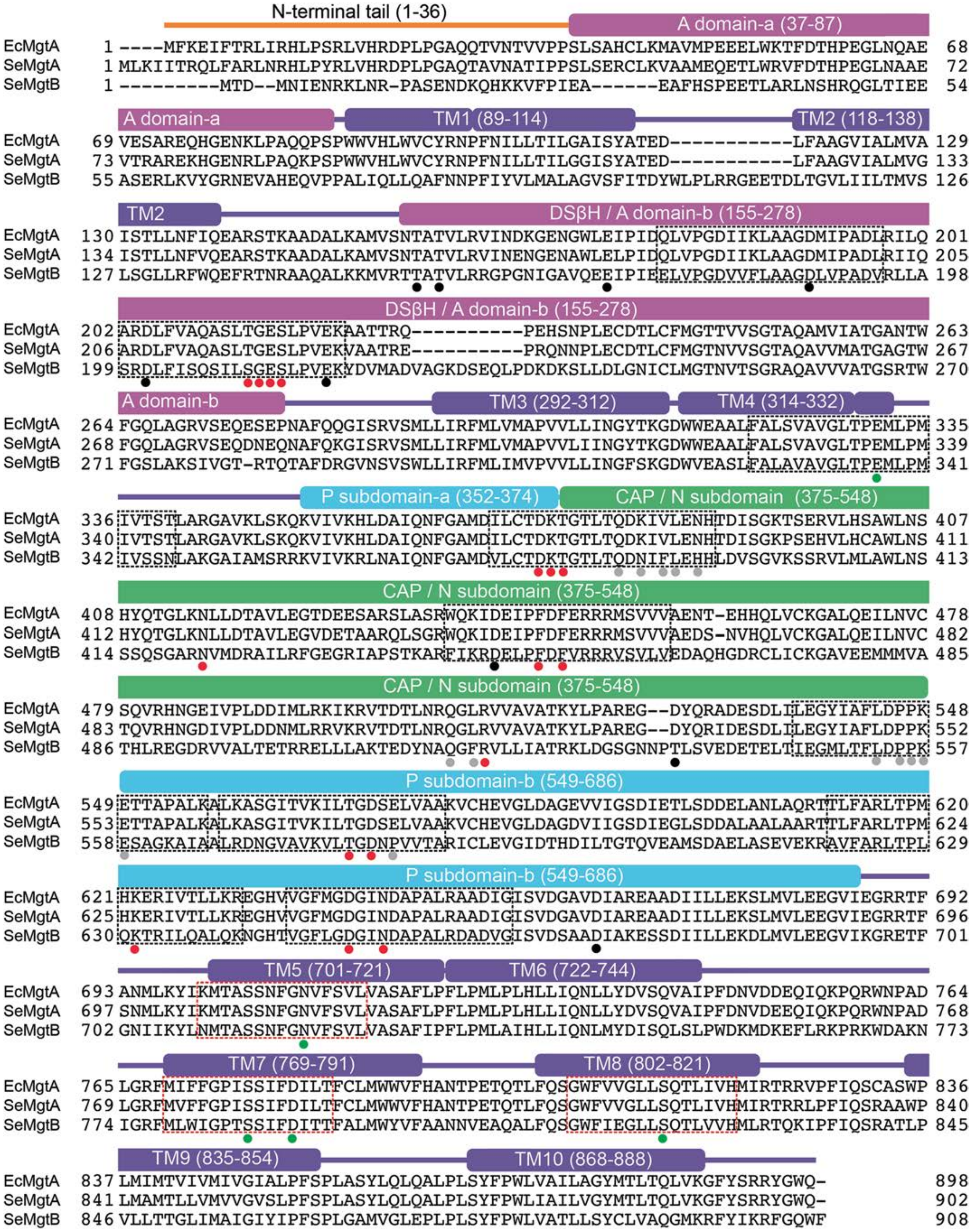

Extended Data Fig. 1 | See next page for caption.

Extended Data Fig. 1 | Multisequence alignment of MgtA and MgtB illustrating conserved structural and functional features. Sequence alignment of *E. coli* MgtA (EcMgtA), *S. enterica* serovar Typhimurium MgtA (SeMgtA), and *S. enterica* serovar Typhimurium MgtB (SeMgtB) generated using Clustal Omega. Domains are colored and named according to Fig. 1. Both the canonical P-type ATPase nomenclature and more detailed description of the fold of the domain with boundaries are given. The soluble A domain is split into two regions: a and b. The b segment of the A domain is comprised of a Double Stranded beta-Helix fold (DSbH). The soluble P subdomain is a noncontiguous segment comprised of two regions a and b that house the key catalytic residues required for phosphorylation. D373 is phosphorylated in EcMgtA. The N or CAP subdomain is a contiguous sequence that binds the nucleotide and aids in catalysis. The P and N subdomains comprise the haloacid dehalogenase (HAD) domain[20]. The TM-spanning alpha-helical regions, as determined by a residue's alpha-carbon position residing, on average, within the hydrocarbon bilayer interior of the molecular dynamics (MD) simulations (+/- 15 Angstroms from the bilayer midplane) are denoted by TM1-10. Gray circles denote residues present at the dimer interface, red circles denote residues near ATP, green circles denote residues near Mg^{2+} in the transmembrane domain, and black circles denote residues near Mg^{2+} in the cytoplasmic domain in our dimeric cryo-EM structures, as annotated in Figs. 2–4. Black dashed boxes indicate sequences conserved across all P-type ATPases as shown in the logos in Extended Data Fig. 2b. Red dashed boxes indicate sequences specific to Mg^{2+} importers as shown in the logos in Extended Data Fig. 7b.

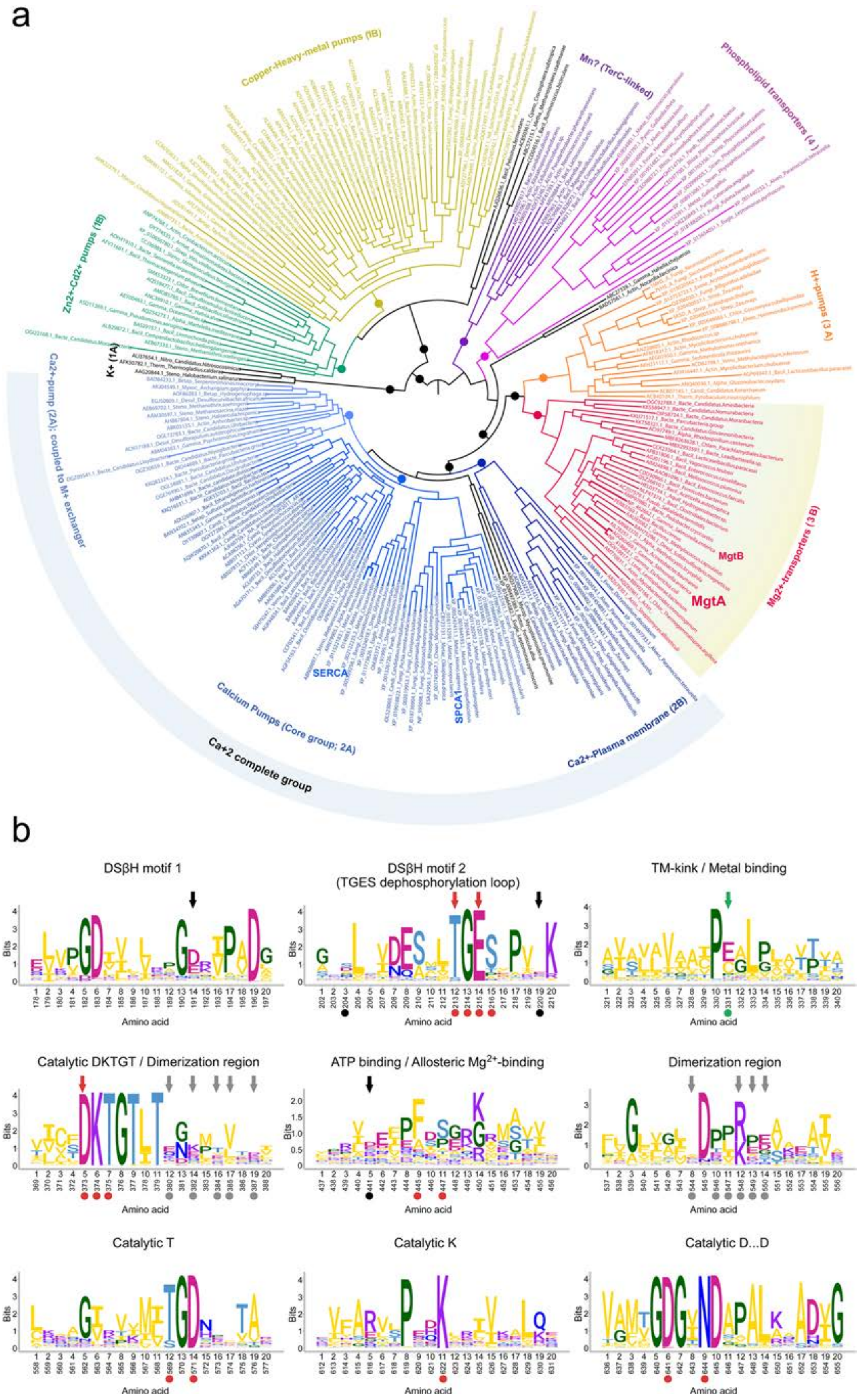

Extended Data Fig. 2 | See next page for caption.

Extended Data Fig. 2 | Tree of P-type ATPases and amino acids related to catalysis and structural architecture that are highly conserved across the P-type ATPase family. a, In the tree, the clades are labeled and colored as per their known or predicted transport substrates. The P-type ATPase subclass is provided in brackets next to the aforestated label. All the major clades with IQtree bootstrap sport of 90% or higher are marked with a filled circle. Branches of special representatives, namely MgtA, MgtB, SERCA and SPCA1 are separately labeled and indicated with bold branches. The tree is based on a multiple sequence alignment of representatives of the major clades of P-type ATPase, which is in figshare. **b**, Sequence logos showing conservation of amino acid residues involved in ATP hydrolysis and structural architecture conserved among entire family of P-type ATPases (indicated by black dashed boxes in Extended Data Fig. 1). Letters represent amino acid abbreviations and height represents the probability of conservation in the P-type ATPase family. As in Extended Data Fig. 1, gray circles denote residues present at the dimer interface, red circles denote residues involved in ATP hydrolysis, green circles denote residues near Mg^{2+} in the transmembrane domain, and black circles denote residues near Mg^{2+} in the cytoplasmic domain in our dimeric structures, as annotated in Figs. 2–4. Gray, red, green and black arrows, respectively, indicate residues located at the dimer interface, involved in ATP hydrolysis, surrounding the transmembrane or cytoplasmic Mg^{2+}, which were mutated in subsequent experiments.

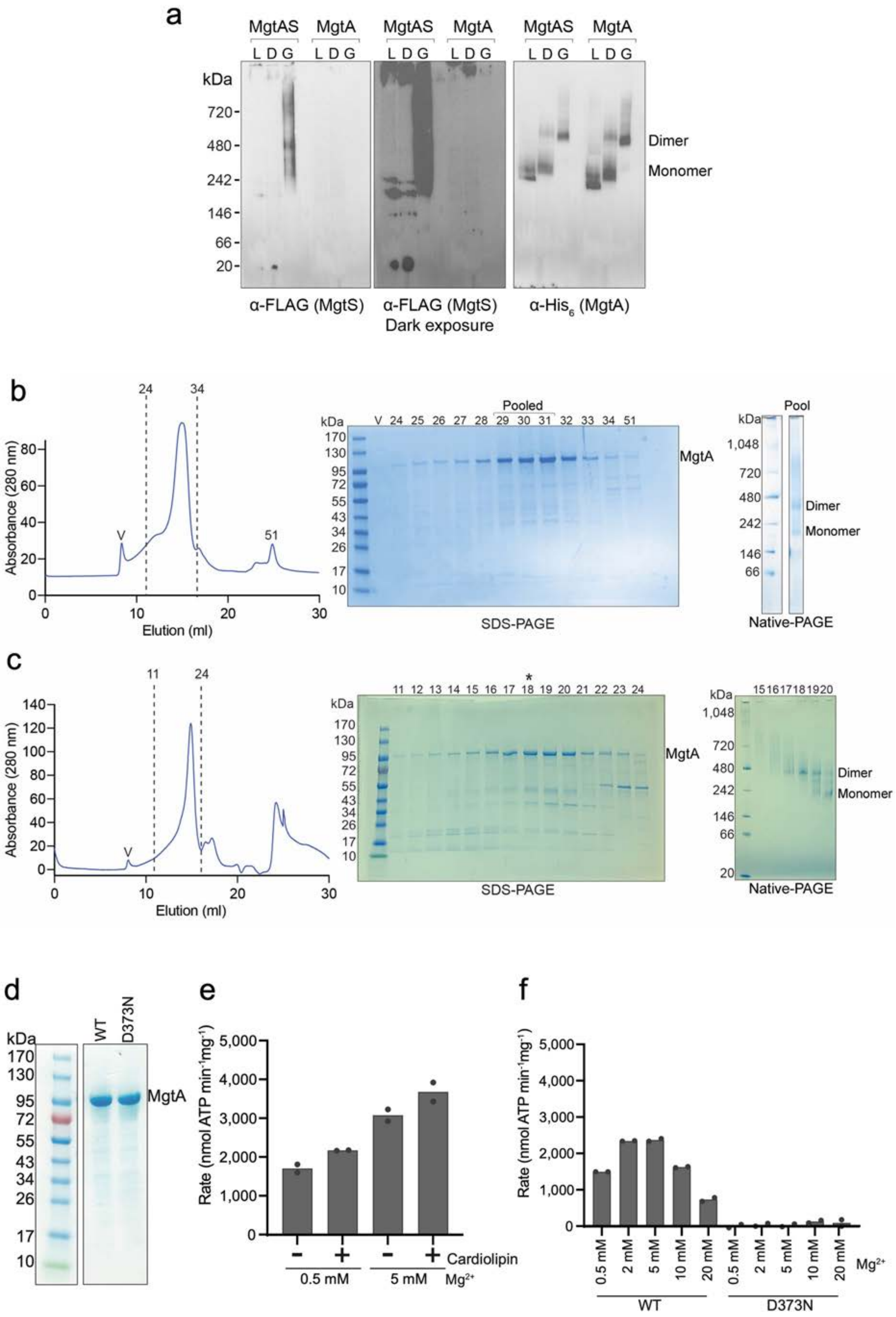

Extended Data Fig. 3 | See next page for caption.

Extended Data Fig. 3 | Purification of MgtA and ATPase activity of purified protein. **a**, Solubilization of membranes expressing MgtA or MgtAS with detergents of varying strengths show differences in native protein interactions when analyzed by Native-PAGE and Western blot analysis. Membranes from cells overexpressing MgtA or MgtAS were solubilized with the detergents LMNG (L), DDM (D), or GDN (G) before Native-PAGE and Western blot analysis using α-FLAG antibodies against tagged MgtS (left two panels; middle panel is a longer exposure of the left panel) or α-His$_6$ antibodies against tagged MgtA (right panel). **b**, Purification of MgtA results in two distinct MW protein complexes. SEC profile (left) of MgtA used to solve the dimer and monomer structures of MgtA in Fig. 1. Fractions were analyzed by SDS-PAGE (middle) and Native-PAGE gels (right). V indicates the void volume of the SEC column. Fractions that were used to solve the structure are referred to as pooled. **c**, Dimeric MgtA can be separated from monomeric MgtA. SEC profile (left) of MgtA used to solve the nucleotide-bound dimer structures of MgtA in Fig. 3 and Supplementary Fig. 3 and 5. Fractions were analyzed by SDS-PAGE (middle) and Native-PAGE gels (right). Fraction 18 which possessed predominantly dimer species was used for structural analysis. **d**, SDS-PAGE gel showing purity of purified WT and D373N mutant proteins assayed in **f**. **e**, ATPase activity of WT MgtA in GDN in the presence of 0.5 or 5 mM $MgCl_2$ and with and without the addition of cardiolipin. **f**, ATPase activity of WT and D373N mutant MgtA in GDN in different concentrations of $MgCl_2$ between 0.5 to 20 mM. For **e** and **f**, protein was purified in 0.5 mM $MgCl_2$ and assays were supplemented with the indicated concentrations of $MgCl_2$. Assays were performed with 6.25 µg MgtA and 2 mM ATP at 37 ° C. Free phosphate was quantified using molybdate/malachite green-based assays (see methods). Data are shown for duplicate experiments with mean. Separate preparations of WT MgtA were assays for **e** and **f**.

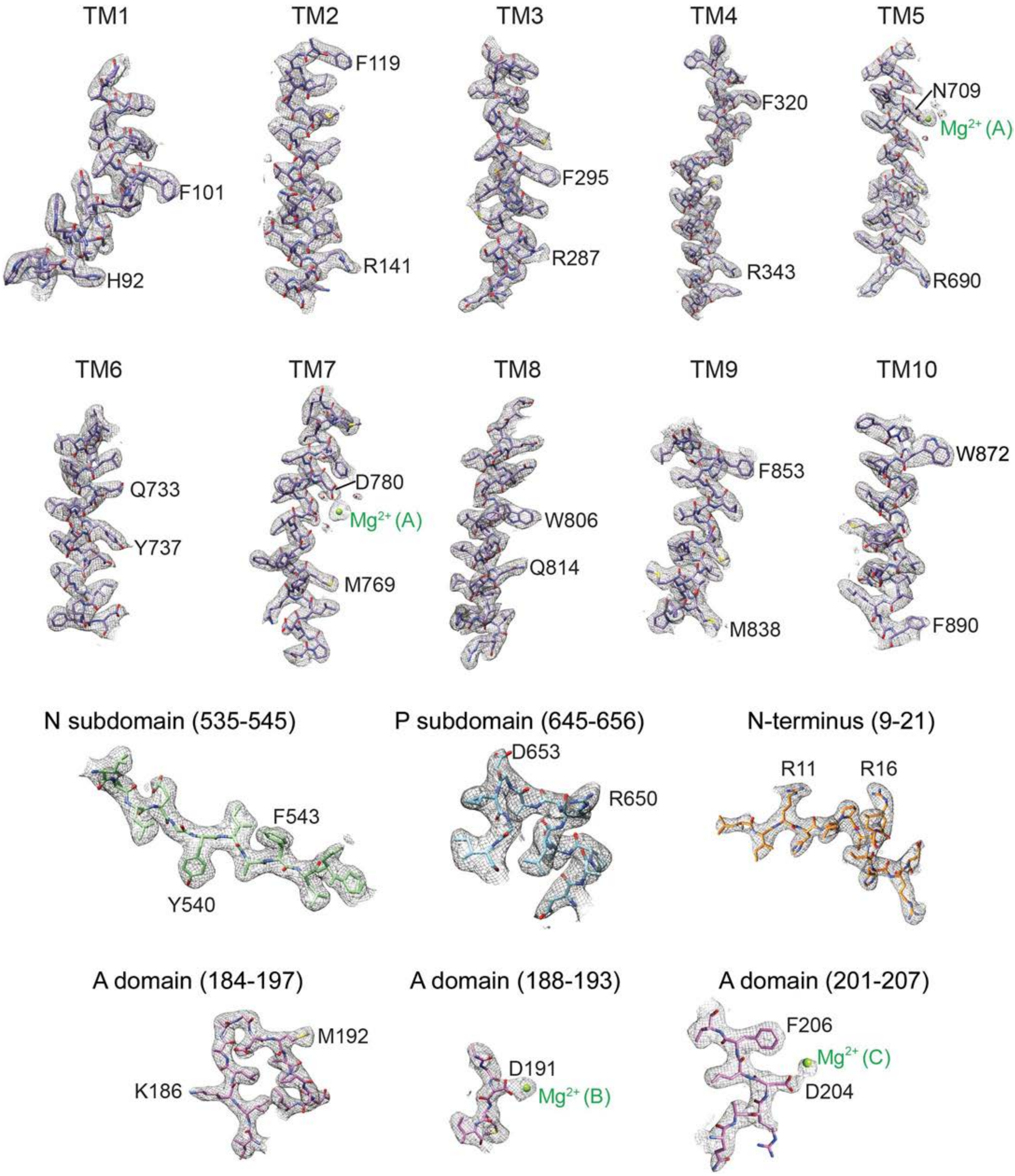

Extended Data Fig. 4 | Quality of cryo-EM dimer map for key structural features. Cryo-EM map and atomic model of the TM segments (1-10), soluble domains (A, P, N), N-terminus, and Mg^{2+} ions colored as in Fig. 1. Atomic model of each structural element is shown in stick representation, the atoms are colored by heteroatom within the cryo-EM map and the corresponding map features are represented in gray mesh.

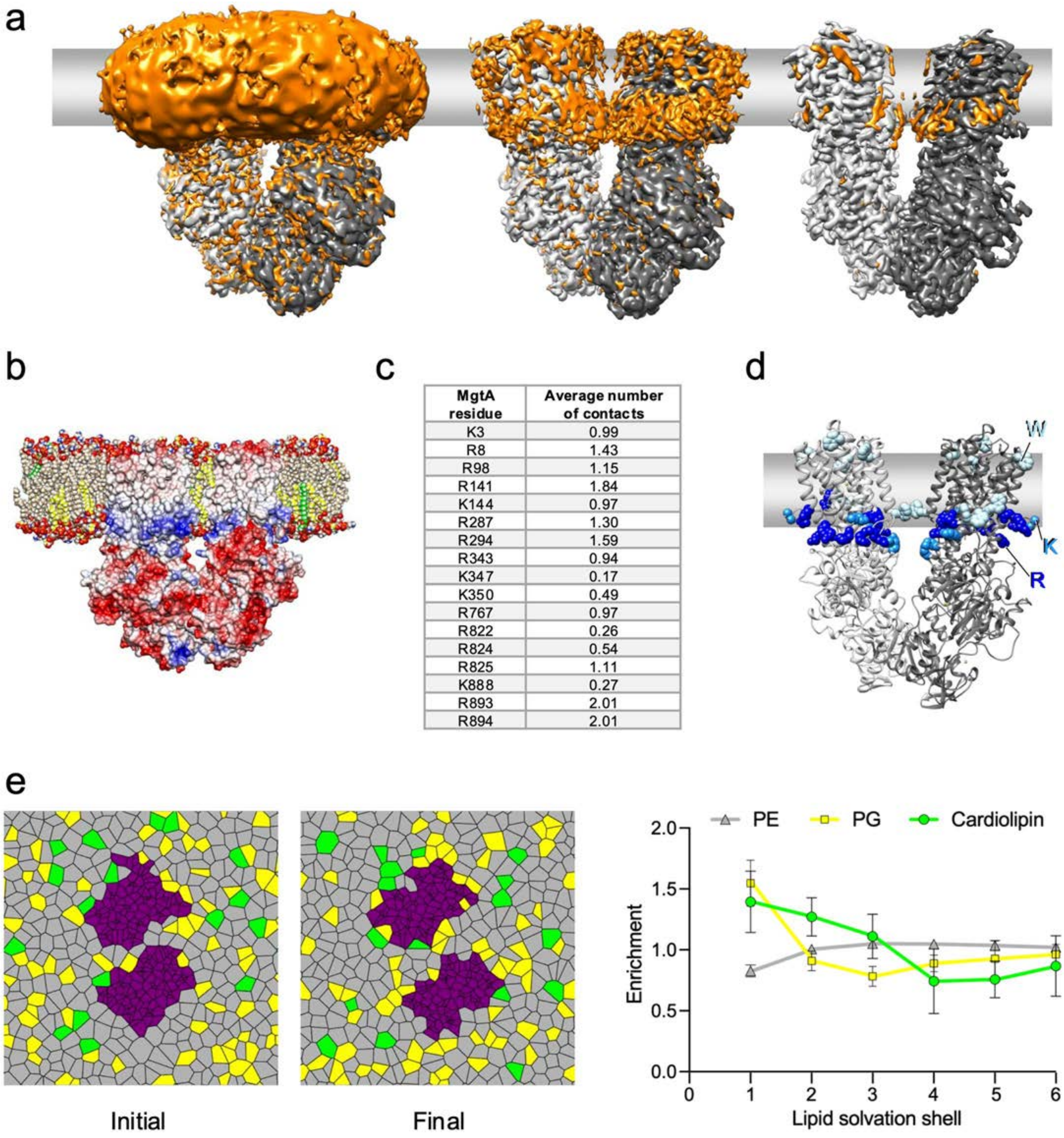

MgtA residue	Average number of contacts
K3	0.99
R8	1.43
R98	1.15
R141	1.84
K144	0.97
R287	1.30
R294	1.59
R343	0.94
K347	0.17
K350	0.49
R767	0.97
R822	0.26
R824	0.54
R825	1.11
K888	0.27
R893	2.01
R894	2.01

Extended Data Fig. 5 | Experimental support of transmembrane borders and lipid distribution. a, Side views of cryo-EM maps at different thresholds showing extra densities in orange corresponding to the detergent micelle, detergent molecules, or potential copurified lipids near the transmembrane region. **b**, Side view of MgtA simulated in a native lipid environment displayed in surface representation colored by electrostatic potential (UCSF Chimera coloring varies from red [-10 kcal/mol/e] to blue [+10 kcal/mol/e] with distance-dependent dielectric constant 4, distance from surface 1.4). Phospholipids corresponding to phosphatidylethanolamine (PE), phosphatidylglycerol (PG) and cardiolipin are colored tan, yellow, and green, respectively. **c**, Arginine and lysine residues that interact with anionic lipids during at least 20% of the simulation, with cutoff enclosing the first peak of the radial distribution function. **d**, Side view of MgtA with arginine (R), lysine (K), and tryptophan (W) residues near the lipid membrane borders highlighted in blue spheres. **e**, Voronoi decomposition of lipid centers-of-geometry in the cytoplasmic leaflet initially (initial) and at the end of the simulation (final). Yellow and green are anionic PG and cardiolipin lipids, respectively. At right, average enrichment or depletion of lipids based on solvation shell as assigned by Voronoi decomposition averaged over the trajectory. Data are shown for independent replicates (n = 10) from the same simulation with mean and standard deviation (error bars) for each solvation shell.

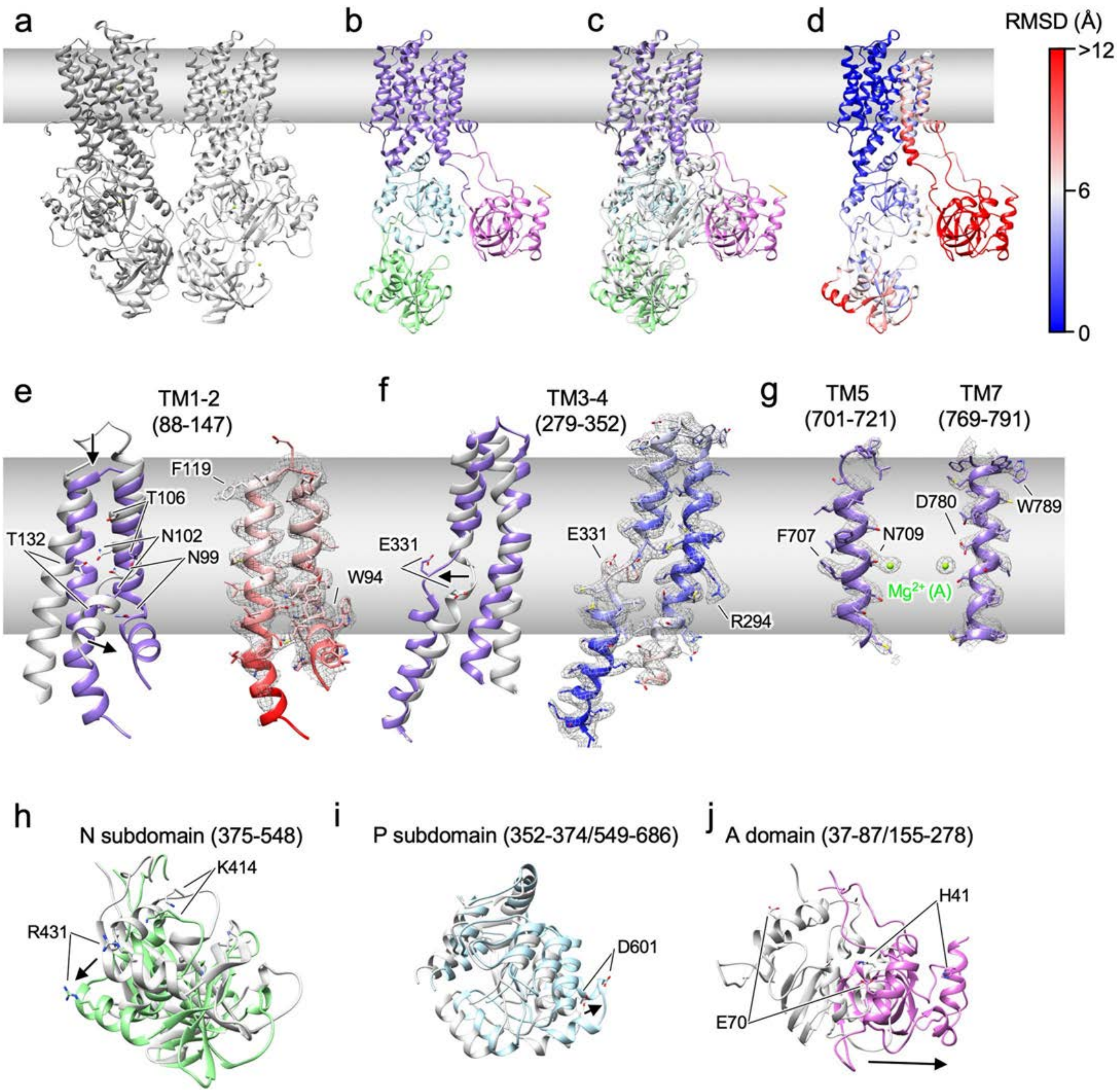

Extended Data Fig. 6 | More splayed conformation of monomeric MgtA structure relative to the dimer with major changes in TM1-4, N and A domains. **a**, Dimeric structure with two subunits in two different gray tones and Mg^{2+} ions as green spheres. **b**, Monomeric structure colored as in Fig. 1. **c**-**d**, To visualize structural changes the colored monomer and a single dimer subunit in gray were superimposed (**c**) and RMSD was calculated (**d**). The monomer structure is shown colored by RMSD indicating the largest differences when comparing the two structures by high RMSD values in red. **e**-**f**, Structural differences between the dimer (gray) and monomer (purple) for TM1-2 (**e**) and TM3-4 (**f**). The monomer colored according to RMSD is on the right with densities in mesh indicating the fit. **g**, Monomer density features and fitted model of TM5 and TM7 near ion-binding site A in the middle of the membrane which is similar to the dimer structures. **h**-**j**, Differences in position in the overall conformation between the soluble domains of the dimer (gray) and monomer (colored).

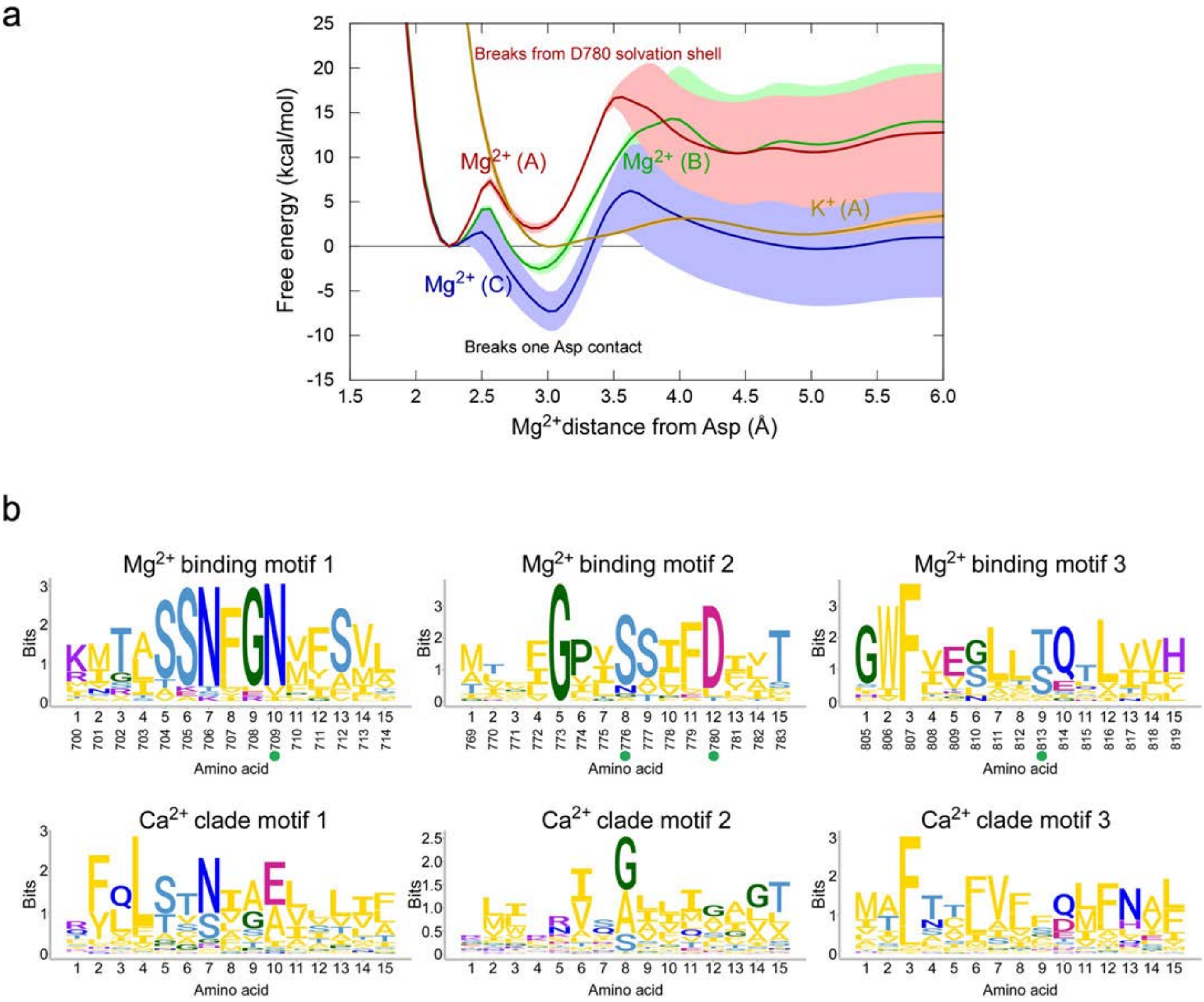

Extended Data Fig. 7 | Stability of Mg^{2+} binding in simulation and conservation of key Mg^{2+}-binding residues. a, Adaptive-biasing MD simulations perturbing Mg^{2+} from the three binding sites and K^{+} from site A. Simulated barriers are similar for Mg^{2+} at each site at 13-15 kcal/mol, with K^{+} much weaker. Data are for independent simulations (n = 3) with mean (colored solid line) and standard deviation (shaded band) indicated. **b**, Sequence logos displaying conservation of amino acids in different members of the P-type ATPase transporters. Letters represent amino acid abbreviations; the height of each letter represents the relative probability of conservation among members of the P-type ATPase family. Logos correspond to the Mg^{2+} TM binding site A to illustrate residues conserved in the MgtA clade (top) compared to the Ca^{2+} clade (bottom). The sequence logos are also highlighted in the reduced multisequence alignment in Extended Data Fig. 1. Green circles denote residues near Mg^{2+} in the transmembrane domain.

https://doi.org/10.1038/s41594-025-01593-7

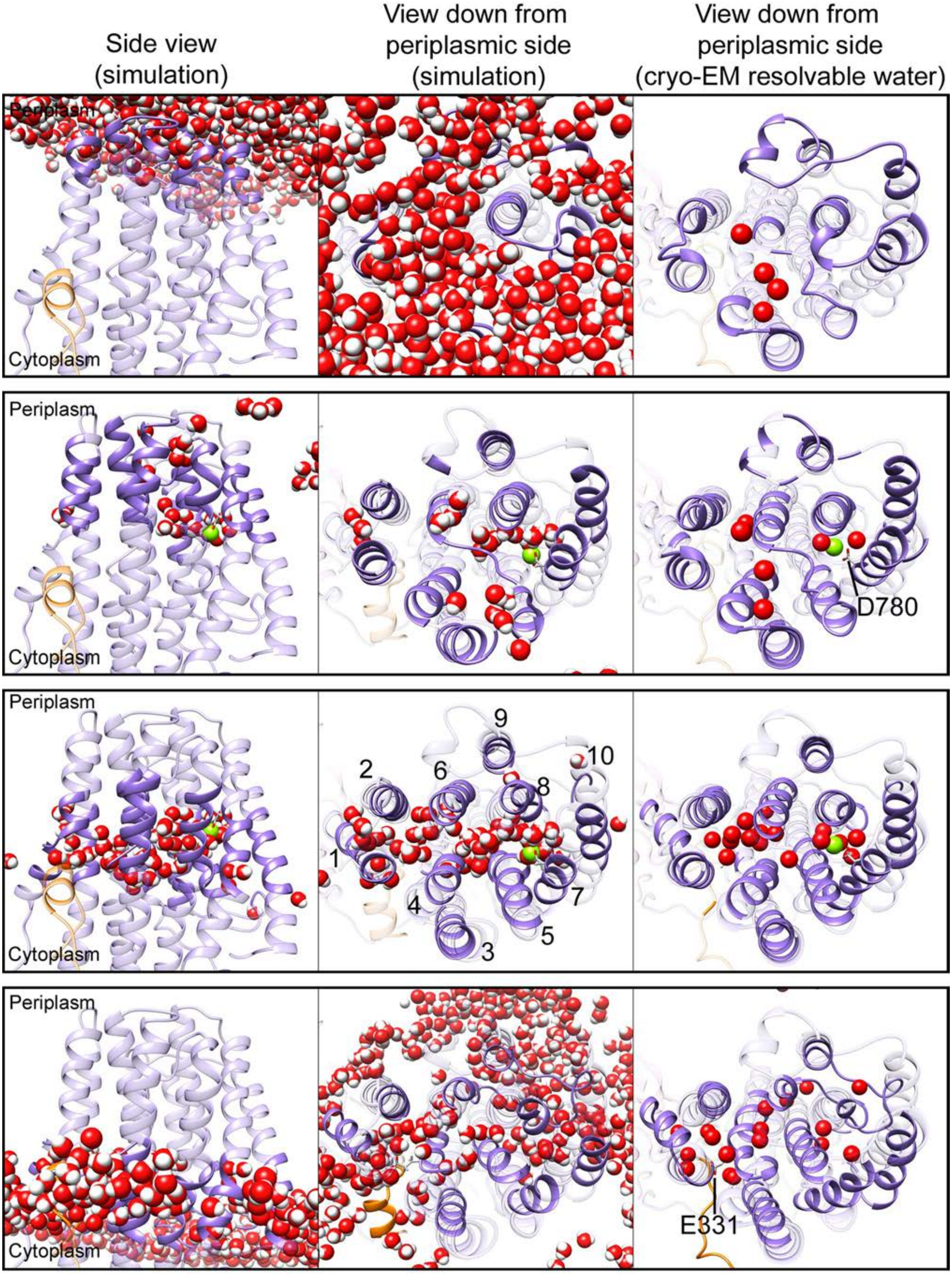

Extended Data Fig. 8 | See next page for caption.

Extended Data Fig. 8 | Water accessibility in the TM domain of MgtA. Figures are arranged such that rows correspond with overlapping 1.5 nanometer thick cuts spaced every 1 nanometer. The left column is the side view from the simulation, while the middle column is from the top-down starting on the periplasmic side of the transporter. For the simulation, waters (including hydrogens) are shown in sphere representation. At right is the corresponding top-down view of the MgtA dimer from cryo-EM, with resolved water molecules shown as red spheres. The protein ribbon model is shown opaque through the cut of the simulation, while outside of the cut waters are not shown, and the protein is transparent. The transmembrane Mg^{2+} is a green sphere and residues E331 and D780 are shown in stick representation.

https://doi.org/10.1038/s41594-025-01593-7

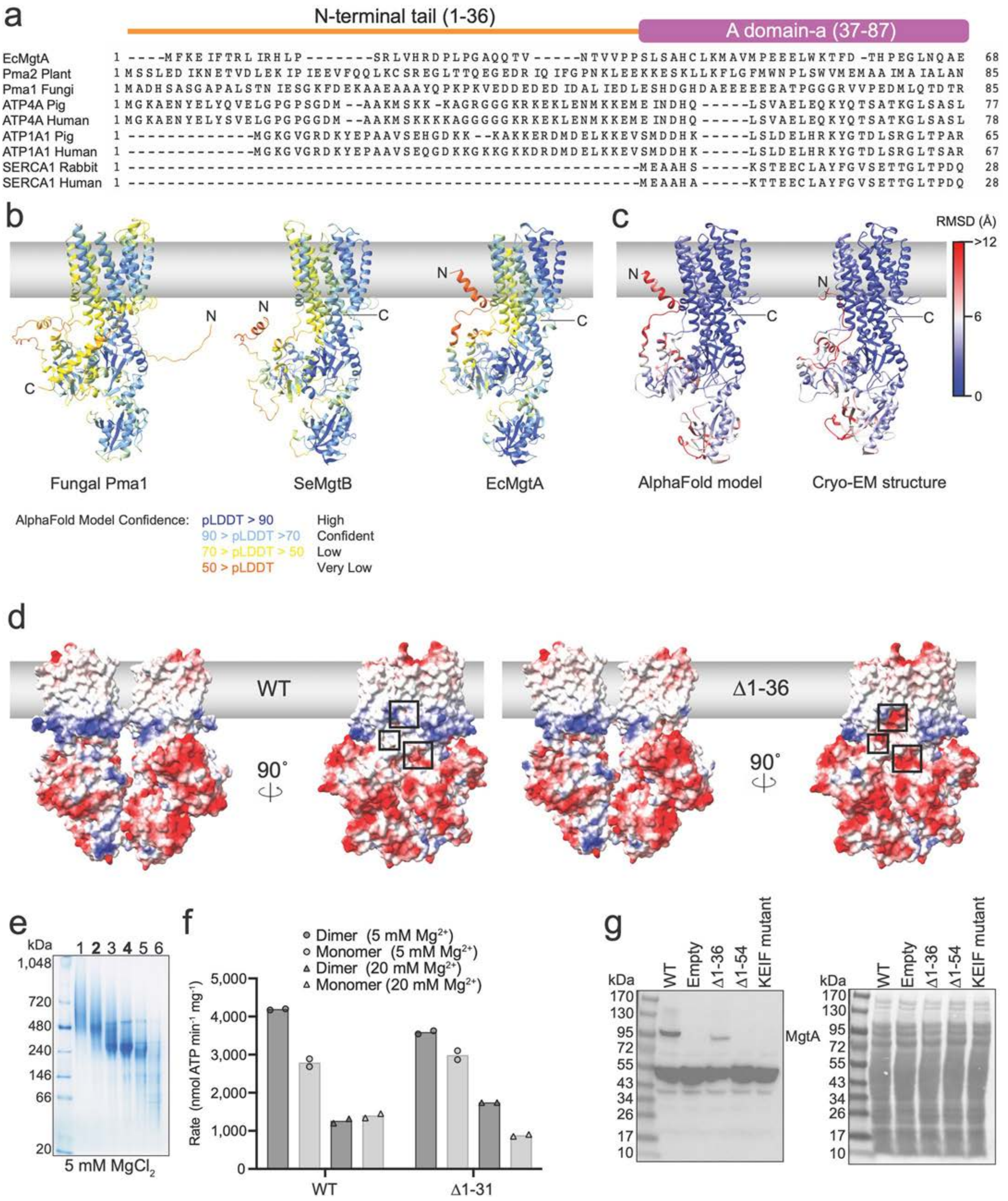

Extended Data Fig. 9 | See next page for caption.

Extended Data Fig. 9 | Extended N-terminus cannot be predicted by AlphaFold, conceals negative patches but does not affect ATPase activity. **a**, Alignment showing extended N-terminus present in MgtA, H^+-pumps, H^+/K^+-ATPases and Na^+/K^+-ATPases but not Ca^{2+}-pump SERCA. The sequence alignment of *E. coli* MgtA (EcMgtA), Plant Pma2, Fungal Pma1, ATP4A (H^+/K^+ transporter) from pig and human, ATP1A1 (Na^+/K^+ transporter) from pig and human, and SERCA (ATP2A1) from rabbit and human was generated using Clustal Omega. Domains are colored and named according to Fig. 1. A more complete alignment can be found in figshare. **b**, AlphaFold models of Fungal Pma1, SeMgtB and EcMgtA. AlphaFold's low confidence score for the N-terminal tails predicts them to be disordered. **c**, RMSD calculated between the AlphaFold model and a single subunit of the dimeric MgtA structure to visualize differences. **d**, Front and side view of the surface representation of the electrostatic potential displayed for WT and the deletion of the N-terminus (Δ1-36). Side view is rotated 90˚. **e**, Native-PAGE gel of SEC fractions 1-6 following Superose 6 fractionation of Δ1-31 in 5 mM $MgCl_2$. Bolded fractions 2 and 5 were used in the ATPase assay. **f**, ATPase activity of dimer and monomer fractions with either 5 mM or 20 mM $MgCl_2$. Assays were performed with 6.25 µg MgtA and 2 mM ATP at 37˚C and free phosphate was quantified using molybdate/malachite green-based assays (see methods). Data are shown for duplicate experiments with mean. **g**, Levels of MgtA are reduced by mutations of the N-terminus, to either eliminate the N-terminus or mutate residues conserved in the Mgt family and suggested to play a role in membrane sensing[29]. Cells were grown uninduced (- IPTG) overnight at 37˚C in LB supplemented with 100 mM $MgSO_4$ and normalized in lysis buffer before western blot analysis with polyclonal anti-MgtA antibodies. Non-specific bands, also observed with just the vector control, are detected with the native antibody for the low levels of MgtA assayed here. Ponceau S-stained membrane (right) serves as a loading control.

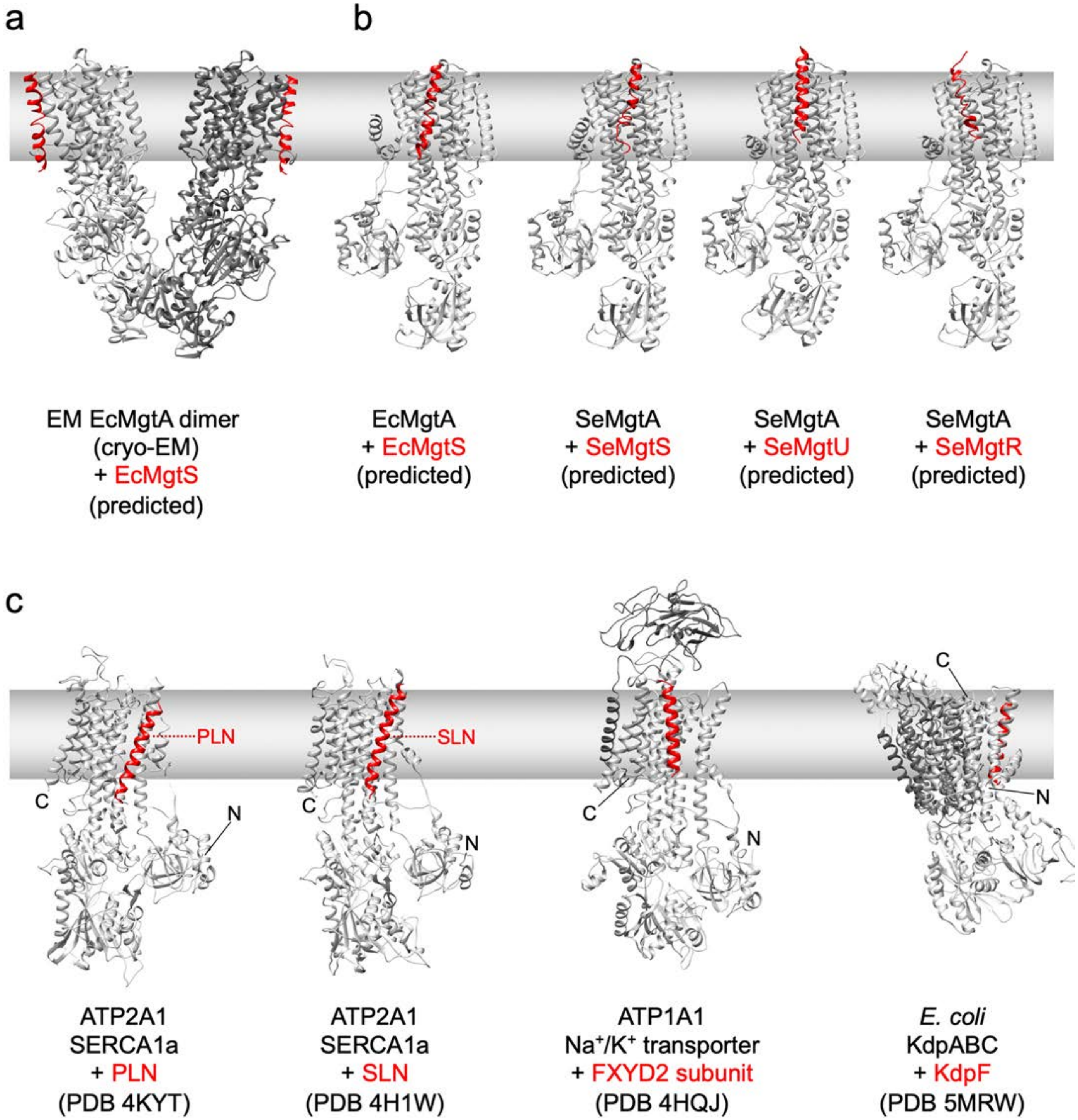

Extended Data Fig. 10 | Predicted and documented interactions of small proteins with P-type ATPase proteins. a, Dimer cryo-EM structure of *E. coli* MgtA from this study with *E. coli* MgtS binding predicted by AlphaFold Multimer beta. **b**, Models of *E. coli* MgtA monomer and *E. coli* MgtS and *S. enterica* MgtA and *S. enterica* MgtS, MgtU and MgtR predicted by AlphaFold Multimer beta. **c**, Selected structures of indicated P-type ATPases solved with small α-helical proteins: SERCA1a + phospholamban (PLN)[48], SERCA1a + sarcolipin (SLN)[22], ATP1A1 + FXYD2 subunit[60], and KdpABC + KdpF[53]. P-type ATPases are in gray with small protein in red.

nature portfolio

Corresponding author(s): Alexander Sodt, Gisela Storz, Doreen Matthies

Last updated by author(s): Jan 9, 2024

Reporting Summary

Nature Portfolio wishes to improve the reproducibility of the work that we publish. This form provides structure for consistency and transparency in reporting. For further information on Nature Portfolio policies, see our Editorial Policies and the Editorial Policy Checklist.

Statistics

For all statistical analyses, confirm that the following items are present in the figure legend, table legend, main text, or Methods section.

n/a	Confirmed	
☐	☒	The exact sample size (*n*) for each experimental group/condition, given as a discrete number and unit of measurement
☐	☒	A statement on whether measurements were taken from distinct samples or whether the same sample was measured repeatedly
☐	☒	The statistical test(s) used AND whether they are one- or two-sided *Only common tests should be described solely by name; describe more complex techniques in the Methods section.*
☒	☐	A description of all covariates tested
☒	☐	A description of any assumptions or corrections, such as tests of normality and adjustment for multiple comparisons
☐	☒	A full description of the statistical parameters including central tendency (e.g. means) or other basic estimates (e.g. regression coefficient) AND variation (e.g. standard deviation) or associated estimates of uncertainty (e.g. confidence intervals)
☒	☐	For null hypothesis testing, the test statistic (e.g. *F*, *t*, *r*) with confidence intervals, effect sizes, degrees of freedom and *P* value noted *Give P values as exact values whenever suitable.*
☒	☐	For Bayesian analysis, information on the choice of priors and Markov chain Monte Carlo settings
☒	☐	For hierarchical and complex designs, identification of the appropriate level for tests and full reporting of outcomes
☒	☐	Estimates of effect sizes (e.g. Cohen's *d*, Pearson's *r*), indicating how they were calculated

Our web collection on statistics for biologists contains articles on many of the points above.

Software and code

Policy information about availability of computer code

Data collection	SerialEM (version 4.1) for CryoEM data collection
Data analysis	CryoSPARC (version 3.2), CisTEM (version 1.0.0), COOT (version 0.8.9.3), PHENIX (version 1.20), CHARMM-GUI (version 3.7) , Amber20 (version 20.0), Tachyon (version 0.98.9), JPred, RoseTTAfold, AlphaFold2, MMseqs, FigTree (version 1.4.4), IQTree (version 1.6.12), MolProbity (version 4.02), MaxQuant software (v2.1.0.0), UCSF ChimeraX (version 1.8), UCSF Chimera (version 1.18), ProteinLynx Global Server 3.0.3, HDExaminer by Sierra Analytics 3..3.0, R-Studio, Chronos 4.9.3, Mass Lynx 4.2, GraphPad Prism version 10.2.1

For manuscripts utilizing custom algorithms or software that are central to the research but not yet described in published literature, software must be made available to editors and reviewers. We strongly encourage code deposition in a community repository (e.g. GitHub). See the Nature Portfolio guidelines for submitting code & software for further information.

Data

Policy information about availability of data

All manuscripts must include a data availability statement. This statement should provide the following information, where applicable:

- Accession codes, unique identifiers, or web links for publicly available datasets
- A description of any restrictions on data availability
- For clinical datasets or third party data, please ensure that the statement adheres to our policy

The data that support this study are available from the corresponding authors upon request. Cryo-EM maps have been deposited in the Electron Microscopy Data

Bank (EMDB) under accession codes EMD-42794 (apo-dimer, C2), EMD-42795 (apo-dimer, C1), EMD-42796 (apo-monomer, C1), EMD-42797 (ATP-dimer, C2), EMD-42798 (ATP?S-dimer, C2), EMD-42799 (ADP-dimer, C2). The atomic coordinates have been deposited in the Protein Data Bank (PDB) under accession codes 8UY7 (apo-dimer, C2), 8UY8 (apo-dimer, C1), 8UY9 (apo-monomer, C1), 8UYA (ATP-dimer, C2), 8UYB (ATP?S-dimer, C2), 8UYC (ADP-dimer, C2); Trajectories and AMBER input files for simulations with and without ATP are publicly available at Zenodo (http://doi.org/10.5281/zenodo.10017395). Calculation of water pathway code is available (https://github.com/alexsodt/WaterPathMGTA). The mass spectrometry proteomics data have been deposited to the ProteomeXchange Consortium via the PRIDE partner repository 85 with the dataset identifier PXD047999. The MgtA (POABB8) and MgtS (A5A616) sequences can be readily downloaded from UniProtKB. The source data for Fig. 2, 3, and 4 and Extended Data Fig. 2 are in figshare (DOI: 10.6084/m9.figshare.26820568).

Research involving human participants, their data, or biological material

Policy information about studies with human participants or human data. See also policy information about sex, gender (identity/presentation), and sexual orientation and race, ethnicity and racism.

Reporting on sex and gender	n/a
Reporting on race, ethnicity, or other socially relevant groupings	n/a
Population characteristics	n/a
Recruitment	n/a
Ethics oversight	n/a

Note that full information on the approval of the study protocol must also be provided in the manuscript.

Field-specific reporting

Please select the one below that is the best fit for your research. If you are not sure, read the appropriate sections before making your selection.

☒ Life sciences ☐ Behavioural & social sciences ☐ Ecological, evolutionary & environmental sciences

For a reference copy of the document with all sections, see nature.com/documents/nr-reporting-summary-flat.pdf

Life sciences study design

All studies must disclose on these points even when the disclosure is negative.

Sample size	For in vivo growth and viability, we performed distinct biological duplicate measurements. Biological replicates are defined as two separate transformants colonies. The data are highly reproducible with little variability from across the entire study. Results are described in the proper qualitative manner. ATPase measurements were performed with distinct replicates as defined as two replicates of measured reagents and reactions. Separate purifications across different weeks have consistent results. These sample sizes are appropriate due to the high reproducibility of measurements and complementary but distinct experimental validations.
Data exclusions	No data were removed from analyses.
Replication	All experiments were independently repeated during the duration of the study with all attempts at replication being successful (performed at least twice).
Randomization	No randomization of samples was used in our study because single-particle cryo-EM analysis is based on randomly distributed single particle subsets. All additional data are supported by multiple lines of complementary but independent experiments to eliminate experimental bias.
Blinding	Investigators were not blinded to this study as no subjective allocation was involved. The investigators performed all experiments with no bias with openly eager anticipation for any resulting outcomes.

Reporting for specific materials, systems and methods

We require information from authors about some types of materials, experimental systems and methods used in many studies. Here, indicate whether each material, system or method listed is relevant to your study. If you are not sure if a list item applies to your research, read the appropriate section before selecting a response.

Materials & experimental systems

n/a	Involved in the study
☐	☒ Antibodies
☒	☐ Eukaryotic cell lines
☒	☐ Palaeontology and archaeology
☒	☐ Animals and other organisms
☒	☐ Clinical data
☒	☐ Dual use research of concern
☒	☐ Plants

Methods

n/a	Involved in the study
☒	☐ ChIP-seq
☒	☐ Flow cytometry
☒	☐ MRI-based neuroimaging

Antibodies

Antibodies used	We used polyclonal MgtA antibody derived from rabbits that were created by LabCorp. The Monoclonal anti-FLAG M2-peroxidase (HRP) antibody produce in mouse is from MilliporeSigma, catalog number A8592. The Penta His HRP conjugated antibody is from Qiagen, catalog number 34460.The polyclonal goat anti-Rabbit IgG secondary antibody conjugated to HRP is from ThermoFisher Scientific, catalog number 32460.
Validation	We validated our primary MgtA antibody at 1:2,500 dilution against a wt and deletion background to confirm that the correct MgtA band is assigned to our protein of interest. Monoclonal anti-FLAG M2-peroxidase (HRP) antibody produce in mouse has a minimum detection of FLAG-Fusion protein (N-BAP) when using 1:100 dilution of conjugate Dot Blot. detection of FLAG-Fusion protein (N-BAP) when using 1:1,000 dilution of conjugate Immunocytochemistry. Anti-Rabbit secondary antibodies are affinity-purified antibodies with well-characterized specificity for rabbit immunoglobulins and are useful in the detection, sorting or purification of its specified target. Pentahis HRP conjugate kit from Qiagen used at 1:1,000. Anti·His HRP. Conjugate Kits consist of the QIAexpress Anti·His Antibodies chemically coupled to the reporter enzyme horseradish peroxidase (HRP). They can be used for highly specific and sensitive, direct detection of any recombinant protein that has an accessible His tag.

Plants

Seed stocks	n/a
Novel plant genotypes	n/a
Authentication	n/a